Withdrawn NIST Technical Series Publication

Withdrawn Publication

Series/Number	NIST TN 1985
Title	A Soot Deposition Gauge for Fire Measurements
Publication Date(s)	March 11, 2018
Withdrawal Date	September 18, 2024
Withdrawal Note	Superseded by updated version

Superseding Publication(s) *(if applicable)*

The attached publication has been **superseded by** the following publication(s):

Series/Number	NIST TN 1985-upd1
Title	A Soot Deposition Gauge for Fire Measurements
Author(s)	Amy Mensch; Thomas Cleary
Publication Date(s)	September 18, 2024
URL/DOI	https://doi.org/10.6028/NIST.TN.1985-upd1

Additional Information *(if applicable)*

Contact	
Latest revision of the attached publication	
Related Information	
Withdrawal Announcement Link	

Date updated: September 18, 2024

NATIONAL INSTITUTE OF STANDARDS AND TECHNOLOGY
U.S. DEPARTMENT OF COMMERCE

NIST Technical Note 1985

A Soot Deposition Gauge for Fire Measurements

Amy Mensch
Thomas Cleary

This publication is available free of charge from:
https://doi.org/10.6028/NIST.TN.1985

National Institute of
Standards and Technology
U.S. Department of Commerce

NIST Technical Note 1985

A Soot Deposition Gauge for Fire Measurements

Amy Mensch
Thomas Cleary
Fire Research Division
Engineering Laboratory
National Institute of Standards and Technology
Gaithersburg, MD 20899

This publication is available free of charge from:
https://doi.org/10.6028/NIST.TN.1985

March 2018

U.S. Department of Commerce
Wilbur L. Ross, Jr., Secretary

National Institute of Standards and Technology
Walter Copan, NIST Director and Under Secretary of Commerce for Standards and Technology

National Institute of Standards and Technology Technical Note 1985
Natl. Inst. Stand. Technol. Tech. Note 1985, 43 pages (March 2018)
CODEN: NTNOEF

This publication is available free of charge from:
https://doi.org/10.6028/NIST.TN. 1985

A Soot Deposition Gauge for Fire Measurements

ABSTRACT

The goal of this exploratory project is to demonstrate the feasibility of a conductometric measurement to determine the time-resolved soot deposition on surfaces in fire environments. Quantitative soot deposition data enabled by this measurement method is lacking in the literature and would be useful to advance fire analysis and fire model development. Laminar flow through a thin rectangular channel with a transverse temperature gradient is used to generate thermophoretic deposition exposures on a target surface. Computational fluid dynamics (CFD) modeling is used to design the channel geometry to have well characterized laminar velocity and temperature profiles. The results predict that fully developed laminar flow and temperature profiles are established by the midpoint of the channel length. The linear temperature gradient between channel walls causes thermophoretic deposition of soot particles on the cold wall of the channel. The channel flow is also modeled with the National Institute of Standards and Technology's Fire Dynamics Simulator (FDS) to generate predictions of soot deposition in the channel. In the experiments particles depositing on the target surface cause an increase in the conductance between the interdigitated electrodes. The change in conductance is measured intermittently before, during and after the exposure using a pico-ammeter and an applied voltage. At the end of the exposure the mass loading of deposited soot is determined by two separate measurement methods, including a gravimetric method and a light transmission method. The relationship between the amount of deposition and the conductometric response is evaluated for both types of mass loading measurements. The gravimetric method produced a more coherent correlation to gauge conductance with less scatter than the transmission method. The measured mass loadings are also combined with measurements of the incoming soot concentration to calculate the overall deposition velocity. The deposition velocity is compared to the theoretically predicted thermophoretic velocity, as determined from the measured temperatures and an estimate of particle size. The deposition velocities derived from the gravimetric method corresponded well with the thermophoretic velocities, but both the vertical and horizontal transmission based deposition velocities generally were lower than the thermophoretic velocities.

Keywords: conductometric gauge; deposition velocity; soot deposition; smoke deposition; thermophoretic deposition.

TABLE OF CONTENTS

List of Tables

List of Figures

Glossary

A	Area
Bi	Biot number (hd/k_{solid})
C	Concentration
d	Thickness
D	Diameter
D_h	Hydraulic diameter [$2WH/(W + H)$]
g	Acceleration due to gravity, 9.8 m/s^2
G	Electrical conductance ($1/R$)
Gr	Grashof number for channel [$g\beta(\mathrm{T}_{\mathrm{hot}} - \mathrm{T}_{\mathrm{flow,outlet}})\rho^2/\mu^2$]
h	Convective heat transfer coefficient
H	Channel height
I	Electrical current
k	Thermal conductivity
K_{th}	Thermophoretic coefficient
Kn	Knudsen number, $(2\lambda_s/D_p)(\mathrm{T_p}/\mathrm{T_s})$
L	Channel length
m	Mass
R	Electrical resistance
Re	Reynolds number for channel ($\rho U_{avg} D_h/\mu$)
SLM	Standard L/min (at standard conditions: 101 kPa and 21 °C)
t	Exposure time
T	Temperature
U	Flow velocity
v	Aerosol particle velocity
V	Voltage
W	Channel width
x, y, z	Global coordinates, where x is channel length, z is channel height

Greek

β	Coefficient of thermal expansion (1/T)
ΔT	Temperature difference
ε/k	Lennard-Jones attractive energy well/Boltzmann constant
λ_s	Gas mean free path at $\mathrm{T_s}$ = 25 °C and atmospheric pressure, 0.065 μm
μ	Fluid dynamic viscosity

ρ	Fluid density
σ	Lennard-Jones hard-sphere diameter
τ	Light transmission
∇T	Temperature gradient ($\Delta T/H$)

Subscripts

avg	Average
dep	Deposition
FDS	Fire Dynamics Simulator
nat. conv.	Natural convection
p	Particle
s	Standard conditions
surr.	Surrounding
th	Thermophoretic

1. Introduction

The physics of soot deposition on surfaces are well understood as being dominated by the following deposition mechanisms: thermophoretic, turbulent and gravitational. The thermophoretic mechanism is driven by a temperature gradient in the gas, which imparts collision energies on aerosol particles that are unequal between the hot and cold sides, resulting in motion opposite to the direction of the temperature gradient. Turbulent deposition results from the turbulent transport often described by an eddy diffusion model. Turbulent eddy diffusion typically subsumes diffusive transport due to Brownian motion. Gravitational deposition, also known as gravitational settling, occurs due to gravitational force and is more significant for large particles, on the order of 10 µm or more, that tend to appear from agglomeration over long time periods, on the order of 30 minutes or more [1]. The Fire Dynamics Simulator (FDS) has implemented a computational scheme for predicting soot deposition in fires due to these mechanisms [1]–[3], but lacks sufficient validation data to assess the performance of the models. In addition, the ability to estimate soot deposition rates in a fire is limited by the challenges of accurately measuring the required input parameters in the fire environment, such as spatial and temporal variations in temperature, velocity, and soot and oxidizer concentrations. Therefore, a deposition gauge allowing for continuous direct measurements of soot mass deposited on compartment surfaces is needed for improved understanding of soot deposition in fires and for model assessment.

Previously, conductometric soot gauges have been developed and tested to monitor soot deposition on diesel engine exhaust filters [4], [5]. The gauges are typically comprised of interdigitated conductive traces printed on an insulating circuit board. Prior to deposition, the electric conductance of the electrodes is very low (high resistance) due to gaps between the conductive traces of each terminal. The height of the conductive traces above the board is considered negligible, and given uniform conditions, deposited particles tend to be distributed randomly across the board. As soot particles deposit, they begin to agglomerate and form connections between the circuit traces, allowing a "leakage" current to flow when a voltage is applied to the terminals. Initially deposits are too sparse to bridge the gaps, and no current is measured until a critical density of particles deposit. After the critical density is reached, the current tends to increase with continued deposition as the density of the soot particles increases. A percolation model to describe this process was developed by Cleary [6].

While the conductometric gauge detects deposition regardless of the driving mechanism, this study focuses on thermophoretic deposition, which has a significant role in fires, especially for small particles (0.1 µm to 1 µm) [7] produced during flaming combustion. A transverse temperature gradient is applied across the height of a rectangular laminar flow channel, ensuring deposition occurs only on the cold side of the channel. To isolate the thermophoretic deposition mechanism the channel is positioned so the flow is vertically downward. In some experiments, the channel is oriented horizontally with the deposit surface facing upward to capture both gravitational and thermophoretic deposition on the same deposit surface. Turbulent deposition is considered negligible because of the laminar condition of the flow.

Thermophoretic deposition is characterized by the average particle velocity generated by the thermophoretic mechanism in the opposite direction of the temperature gradient, ∇T. The thermophoretic velocity, v_{th}, is proportional to ∇T and related to properties of the gas and particle, as given in Eq. (1).

$$v_{th} = -K_{th}\frac{\mu\nabla T}{\rho T_p} \tag{1}$$

K_{th} is the thermophoretic coefficient, which in general depends on particle size and Kn. For Kn >> 1, when the mean free path of the gas is much greater than the particle size, K_{th} is generally assumed to be 0.55 and independent of particle size [8]. This condition is known as the free molecular regime. K_{th} can also be calculated as a function of Kn, the thermal conductivities of the gas and particle, and empirical constants [9]. Studies of soot agglomerates have generally found that K_{th} should be evaluated using the primary particle diameter [8], [10], [11], suggesting the use of K_{th} = 0.55 for soot. Suzuki et al. [11] noted that K_{th} also depends on the morphological characteristics of the agglomerates, with more open structures being closer to the free molecular regime compared with more compact agglomerates.

The v_{th} is the same as the overall deposition velocity, v_{dep}, if the force from thermophoresis is uniform and the only significant mechanism driving particles to deposit (diffusion is negligible), and if the main flow is steady, parallel to the deposition surface and contains a steady concentration of particles, C_p. The v_{dep} can be calculated from the mass of deposition, m_{dep}, the exposure area, A_{dep}, the exposure time, t, and incoming C_p in Eq. (2).

$$v_{dep} = \frac{m_{dep}}{C_p A_{dep} t} \tag{2}$$

2. Flow and Heat Transfer Modeling

2.1 Modeling Methods

The flow and heat transfer expected in the channel were modeled using the CFD solver in Comsol for steady state laminar flow, flow heat transfer, and solid heat conduction within the surrounding walls. To minimize flow and thermal development length in the channel, the height of the channel was 1 cm. Initially, two-dimensional simulations were run, progressing to three-dimensional simulations with 1 m flow length, and then simulations of the final channel dimensions, 8 cm wide by 41 cm long. In unsteady simulations, it was found that steady state for the flow velocity and temperature was achieved in 10 s of simulation time. The final channel geometry, including all the domains modeled in the simulations, is depicted in Fig. 1a.

The purple area in Fig. 1a shows the flow domain, with flow entering through the square inlet on the left of the figure, and exiting through the square outlet on the right of the figure. The flow passes through a plenum before and after the flow channel to minimize entrance and exit effects. To further decrease entrance effects, a 6.4 mm diameter rod was inserted across the width of the inlet plenum, intercepting the inlet jet 25.4 mm into the plenum. The origin of the geometry is depicted at the center of the channel inlet plane. The flowrates studied include nominally 3 L/min and 10 L/min at standard conditions 101 kPa and 21 °C, hereafter referred to with the units, SLM. The flow was confirmed to be laminar by calculating the Re based on the hydraulic diameter, D_h. The Re was less than 230 for all cases. The flow boundaries are thermally coupled to the adjacent solid domains, and all other boundaries of the flow domain are adiabatic.

The solid domains include the deposition target boards made of FR-4 circuit board material (k_{target} = 1.06 W/m-K), which are in red in Fig. 1a, and the solid aluminum channel walls and resistance heaters (k_{alum} = 238 W/m-K), which are transparent in Fig. 1a. No additional thermal resistance is added for the interfaces between adjacent solids, such as between the target boards and the cold aluminum wall or between the resistance heaters and the hot aluminum wall. The hot and cold aluminum walls extend the length of the channel and are 10.16 cm wide and 1.91 cm thick. The FR-4 target boards are 10.16 cm wide and 1.59 mm thick. The locations and geometries of the resistance heaters in the simulations match the actual geometry used in the experiments. Each heater is 3.81 cm wide by 30.48 cm long and 8 mm thick. They are centered on top of the hot wall with a 6.4 mm gap between the two heaters. The boundary conditions for all the external boundaries of the solid domains are natural convection ($h_{nat.\ conv.}$ = 5 W/m^{2}K with T$_{surr.}$ of 30 °C), except for the bottom boundary of the cold wall. The external surface of the cold wall is set to a constant temperature of 20 °C to estimate the boundary condition for the serpentine water cooling loop on this surface in the experiments. The power input of the resistance heaters is applied through a uniform heat generation within the heater domains. The steady-state heater power applied in the simulations was determined based on the power required to approximate the desired temperature gradient in the channel.

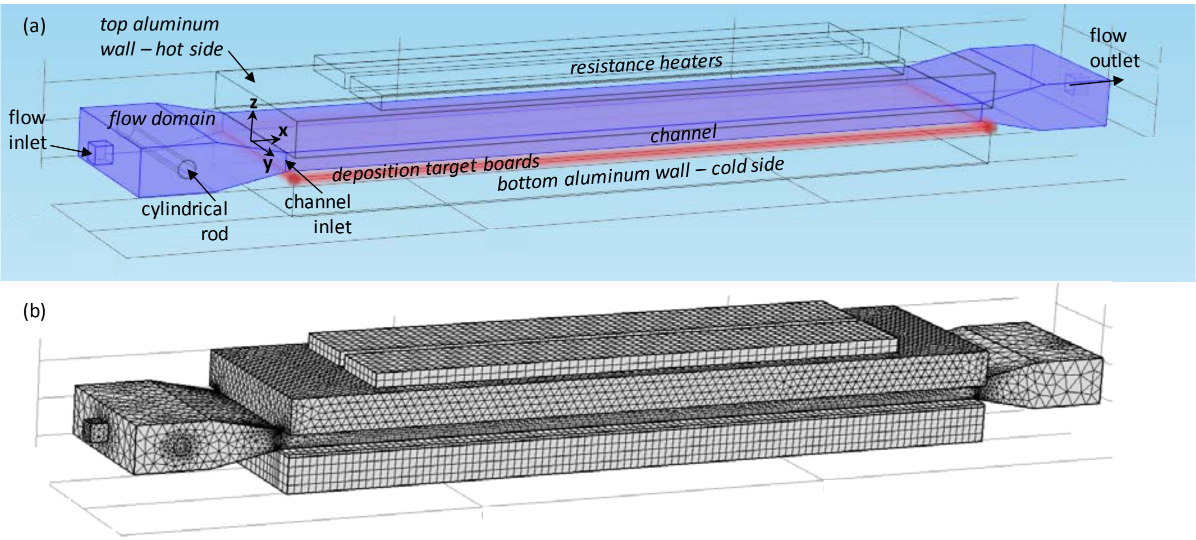

Fig. 1. Flow and heat transfer simulation (a) computational domains and (b) computational grid.

The computational grid, which is comprised of 155,000 cells, is depicted in Fig. 1b. Rectangular structured grids were generated within the deposition target board domain, the bottom aluminum wall, and the aluminum heaters as shown in the close-up view in Fig. 2. Fully unstructured tetrahedral grids were used for the top aluminum wall and the inlet and outlet flow regions. The grid for the flow within the channel, shown in Fig. 2, has three wall-normal prism layers on the top and bottom channel walls to resolve gradients. The prism layers blend into an unstructured tetrahedral grid for the core of the channel flow. The cells in the channel are approximately 1 mm thick in the z-direction, and up to 7.5 mm in the other directions. The largest grid sizes occur in the inlet and outlet sections, and are 10.2 mm at a maximum.

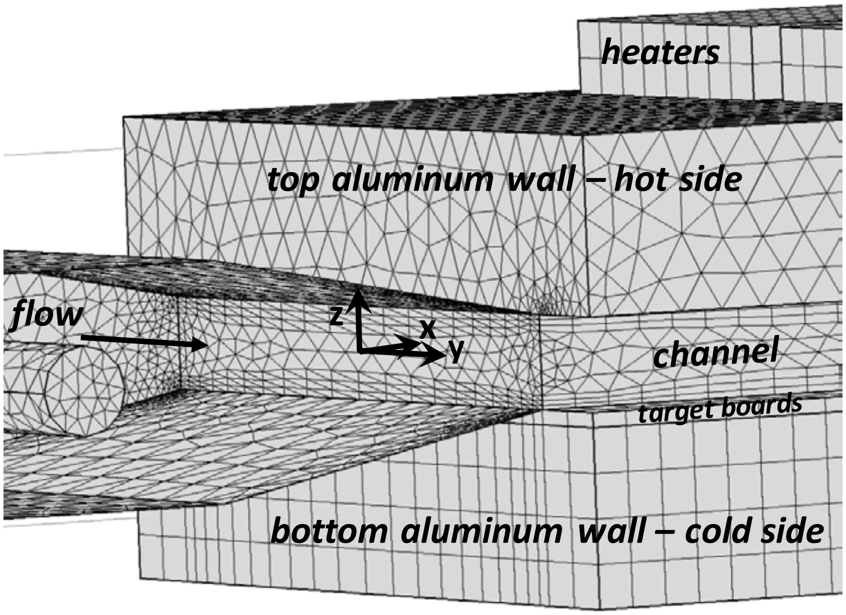

Fig. 2. Close-up view of channel computational grid for flow and heat transfer simulation.

2.2 Experimental Methods Without Deposition

Steady-state flow experiments with heating and cooling but without deposition were performed to measure flow and surface temperatures and determine the heater set point. The experimental channel had the same dimensions as the simulations previously discussed. The side walls of the channel were sealed with polytetrafluoroethylene and two layers of 3.2 mm thick ceramic paper fiber insulation, to minimize heat conduction between the hot and cold walls. Both horizontal and vertically downward orientations were tested. The inlet and outlet flow, and both the hot and cold wall surfaces were instrumented with K-type thermocouples. A thermocouple in the inlet plenum just downstream of the cylinder was used to measure the inlet flow temperature for the computational simulations. The outlet flow thermocouple was positioned in the center of the outlet plenum. K-type thermocouples (bead diameter of 0.025 mm) were adhered with polyimide tape to the top and bottom of the interior of the channel to measure the temperature difference across the channel, ΔT, at three locations along the centerline, x = 0.148 m, 0.249 m and 0.351 m from the channel inlet. Figure 3 depicts the partially assembled channel without the inlet plenum, and shows the locations of the hot and cold side thermocouples adhered to each surface.

Ambient air was pulled into the channel through the inlet plenum. The flowrate was manually controlled by a needle valve and measured by a flowmeter (thermal anemometer type) installed downstream of the channel flow. The calibrated flowrates were 3.3 SLM, and 10.5 SLM, with variations during each experiment less than 5 %. The flowrates are referred to by the nominal rates of 3 SLM and 10 SLM. The average channel velocities based on the measured flowrates were 0.075 m/s for 3 SLM and 0.24 m/s for 10 SLM. The heater power was switched fully on and off by a controller using input from a thermocouple measuring the temperature on the outside of the hot wall. To achieve channel ΔT of 200 °C and 100 °C, the controller set point temperatures were 230 °C and 120 °C respectively. The controller deadband was set to 0.1 °C, resulting in peak to peak oscillations in the outside hot wall temperature of 6 °C to 9 °C, but consistent within experiments.

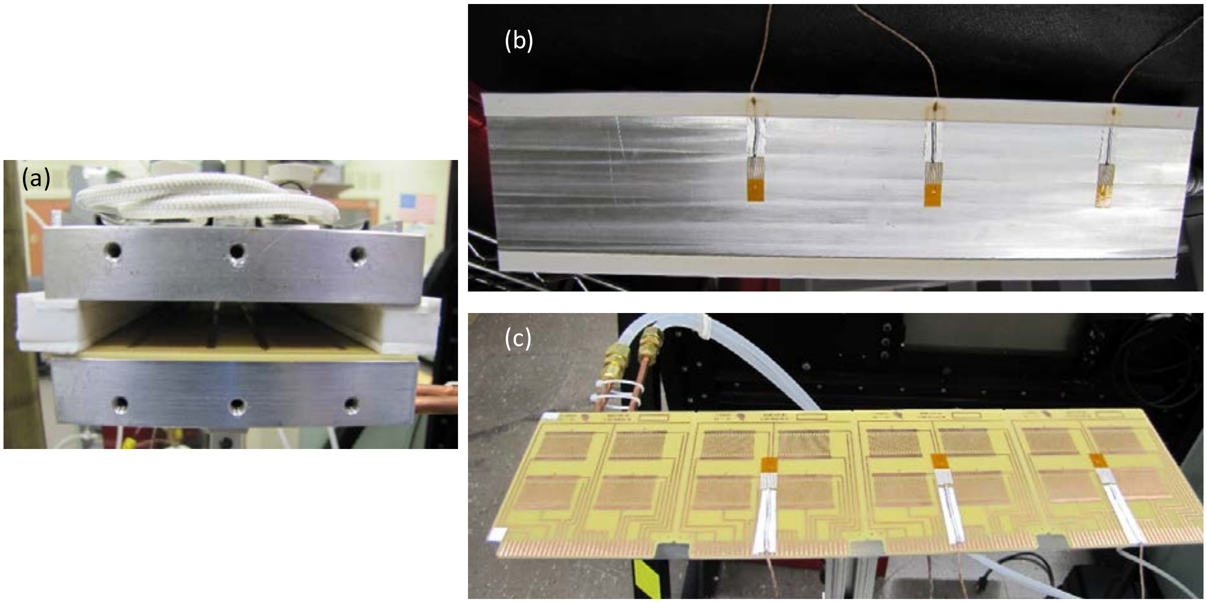

Fig. 3. Photographs of the channel showing (a) the view looking through the inlet without plenums attached, (b) the locations of the hot surface thermocouples, and (c) the locations of the cold surface thermocouples. Flow is left to right.

Table 1 shows the measured flow inlet temperatures and average wall temperatures at the hot side surface of the channel, T_{hot}, for the cases of horizontal and vertical orientation, ΔT of 200 °C and 100 °C, and flowrates of 3 SLM and 10 SLM. Initially in the simulations, the temperature of the flow entering the plenum was assumed to be 30 °C. However, the experiments revealed inlet flow temperatures often greater than 30 °C, depending on the conditions. Although the flow entering the channel was not directly heated, upstream heating occurred from the surrounding aluminum housing that gained heat from the hot wall.

The inlet flow temperatures were higher for the vertical orientation compared to horizontal due to the combined conduction and external natural convection heat transfer in the vertical orientation, while only conduction contributed to upstream heating in the horizontal orientation. It is important to note that natural convection was not expected to affect the internal flow for either the horizontal or vertical orientation. For the horizontal orientation, there was no driving force for natural convection due to the stable temperature gradient in the channel. For the vertical orientation, natural convection was considered negligible based on the criterion of $Gr/Re^2 << 1$. The Gr/Re^2 is estimated to be at most 0.006. The flowrate had a slightly smaller effect on the inlet flow temperature, with lower inlet temperatures observed for the higher flowrate cases because of increased forced convective heat transfer associated with higher flow velocities.

Because the simulations modeled the flow at steady-state, it was necessary to apply a constant power to the heaters in the simulation. Since the average steady-state heater power in the experiments was unknown, the conditions of the simulations and the experiments were matched by the overall temperature difference resulting from a given heat input. The amount of heat applied for each simulation is shown in the bottom row of Table 1.

As a result of the measured inlet flow temperatures, the flow and heat transfer simulations were updated to reflect the measured flow inlet temperatures and the actual calibrated flowrates. The predicted average T_{hot} results are shown in Table 1. Because natural convection in the channel was negligible, the simulations did not account for the orientation of the channel with respect to gravity, except to prescribe a different inlet flow temperature according to the measurements. The predicted values of T_{hot} are slightly higher than the measured values, but follow the same trends as the measured values. The differences can be attributed to the estimates of the steady-state heater power, as well as the estimates of the heat losses to the surroundings through assumptions of $h_{nat.\ conv.}$ and T_{surr}.

Table 1. Experimental and Simulation Flow and Temperature Conditions

Orientation	Horizontal				Vertical			
Approx. Channel ΔT (°C)	200	200	100	100	200	200	100	100
Approx. Flowrate (SLM)	10	3	10	3	10	3	10	3
Measured Flow Inlet T (°C)	50	55	30	34	59	66	41	43
Measured Flow Outlet T (°C)	73	85	43	49	108	80	69	49
Measured Average T_{cold} (°C)	21	23	13	14	21	22	13	13
Measured Average T_{hot} (°C)	216	219	116	116	218	219	117	117
Simulated[a] Average T_{hot} (°C)	218	234	124	132	221	235	125	133
Simulation Heater Power (W)	100	100	50	50	100	100	50	50

[a] Simulated vertical T_{hot} does not account for natural convection, but uses the measured flow inlet T.

The measurements of surface temperature on the cold side of the channel, T_{cold}, are also listed in Table 1. The temperatures on the cold side of the channel and on the external side of the aluminum are expected to be close because of the high conductivity of the aluminum and the small thickness of the FR-4 boards. The Bi number of the boards was estimated and found to be less than 0.1. T_{cold} and T_{hot} are used to verify the overall temperature differences and to calculate the temperature gradients in the channel for the thermophoretic deposition velocity calculation, as discussed in Sec. 4.3.

2.3 Modeling Results

The temperature and velocity results of the final simulations are given in Figs. 4 – 10 for the cases with approximate channel ΔT of 200 °C and both channel flowrates. The flow inlet temperatures are those corresponding to the measurements from the horizontal orientation given in Table 1. The distribution of predicted T_{hot} is given in Fig. 4. The highly conductive aluminum block that forms the top wall of the channel results in a nearly uniform surface temperature for both flowrates. For 3 SLM, a small variation in T_{hot} is visible; T_{hot} increases until just over halfway down the channel, then begins decreasing again until the end of the channel. The temperatures are higher in the middle of the channel because the heaters do not extend the full channel length, and there are heat losses from the inlet and exit of the channel. The peak temperature is located slightly downstream of the midpoint of the channel because the flow is not fully developed at the start of the channel. The heat transfer coefficient is highest at the start of the channel, and then decreases as the thermal boundary layer increases moving downstream. T_{hot} for 10 SLM is about 13 °C cooler than T_{hot} for 3 SLM because the inlet temperature is lower for 10 SLM, and the higher flowrate also leads to higher heat transfer. The variation in the minimum, maximum and average T_{hot} with different heater power inputs is given in Fig. 5. As the heater power increases, the difference between the minimum and maximum temperatures stays small relative to the temperatures themselves, so T_{hot} can be considered uniform throughout the channel.

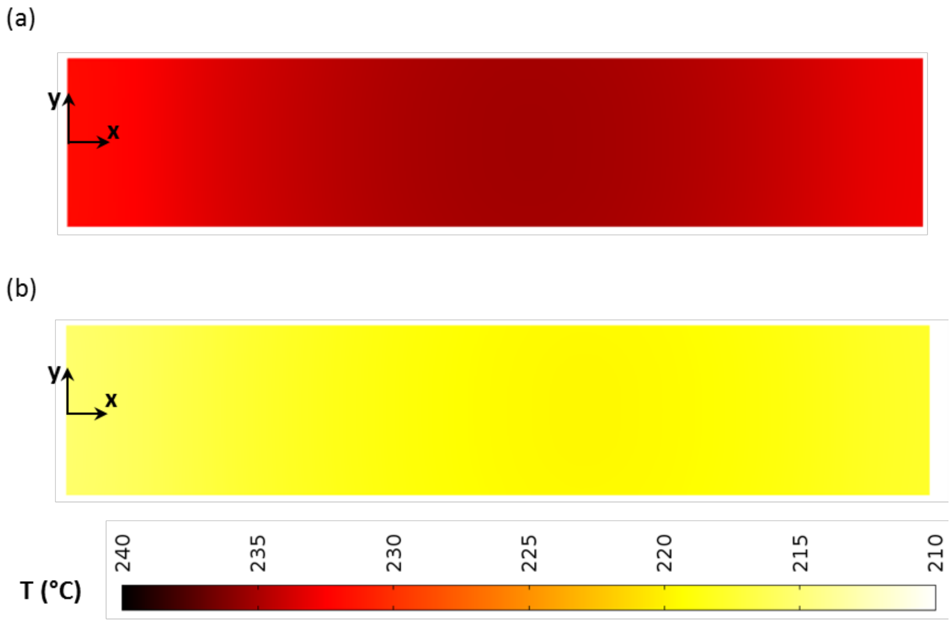

Fig. 4. Surface temperatures at the interface between the channel and the heated upper block for 100 W heater input (ΔT ≈ 200 °C) for (a) 3 SLM, with average T_{hot} = 234 °C, and (b) 10 SLM, with average T_{hot} = 218 °C.

The simulation boundary condition for the external cold wall was set to 20 °C for the cases with ΔT ≈ 200 °C and 12 °C for the cases with ΔT ≈ 100 °C. Figure 6 shows the T_{cold} predicted by the simulations for both flowrates, ΔT ≈ 200 °C, and flow inlet temperatures corresponding to the horizontal cases. T_{cold} is predicted to be very uniform with little variation across the surface. The average T_{cold} predictions are the same as the external boundary conditions, 21 °C for ΔT ≈ 200 °C and 12 °C for ΔT ≈ 100 °C. With the hot and cold side surface temperature predictions, the ΔT is confirmed to be approximately 200 °C for the 100 W cases, and approximately 100 °C for the 50 W cases.

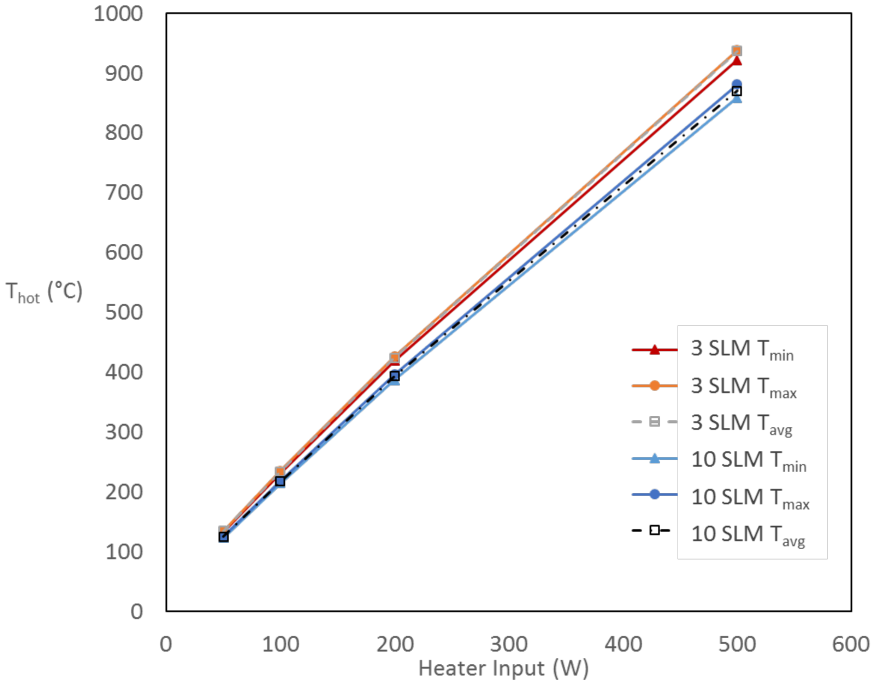

Fig. 5. Minimum, maximum and average simulation surface temperatures at the interface between the channel and the heated upper block as a function of heater power input for 3 SLM and 10 SLM.

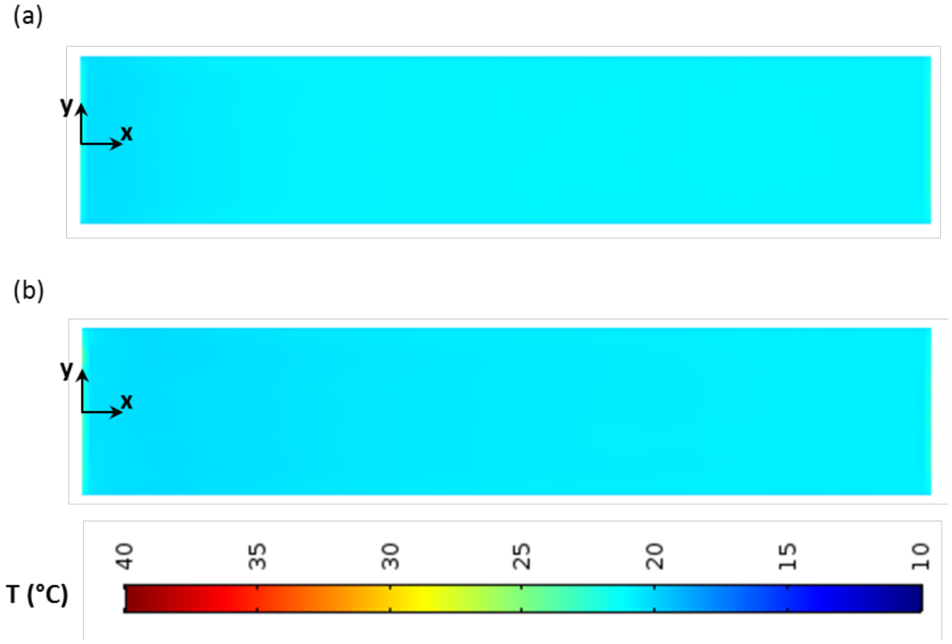

Fig. 6. Surface temperatures at the target surface (above cooled lower block) for the case of heater input of 100 W (ΔT ≈ 200 °C) and a flowrate of (a) 3 SLM, with average T_{cold} = 21 °C, and (b) 10 SLM, with average T_{cold} = 21 °C.

The channel velocity is depicted in Fig. 7 for ΔT ≈ 200 °C and for both flowrates, with slices of streamwise velocity overlaid with streamlines. For each flowrate, two slices of velocity contours are shown. The slice through the mid-width of the channel (top) shows the velocity profile across the channel height. The slice through the mid-height of the channel shows the velocity across the channel width. As expected, there is relatively little variation in velocity across the width except for thin boundary layers at the sides of the channel. All slices also show the transition from the small rectangular inlet, around the cylindrical rod and into the channel, and the corresponding changes in velocity and bending of streamlines. Within the channel, the velocity and streamlines are relatively unchanging in the streamwise direction. For the case of 10 SLM in Fig. 7b, there are small increases in the velocity and in the boundary layer thickness in the upstream portion of the channel.

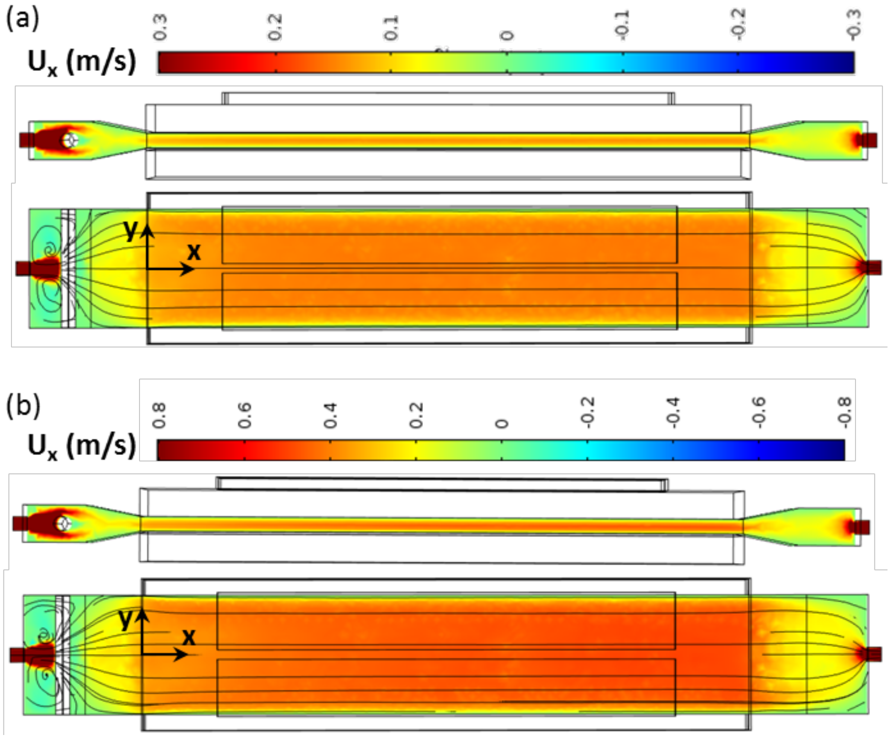

Fig. 7. Contours of streamwise velocity and streamlines at the mid-width of the channel and the mid-height of the channel for heater input of 100 W (ΔT ≈ 200 °C) and flowrates of (a) 3 SLM, and (b) 10 SLM.

The location at which the 10 SLM flow becomes fully developed flow can be found through the centerline velocity profiles across the channel height plotted in Fig. 8. Ten profiles are shown at different distances from the inlet of the channel, from x/L = 0 to just before the end of the channel at x/L = 0.93. The markers plot the values at the gridpoints in the simulation connected by a smooth line to visualize the profiles. The final three profiles lie on top of one another, and the profiles from x/L = 0.29 cm to 0.66 cm are within 5 % of the final profiles. Therefore, the flow can be considered fully developed by 29 % of the channel length or 12.0 cm for the 10 SLM flow case. For 3 SLM, the flow is fully developed farther upstream, at 13 % of the channel length or 5.5 cm.

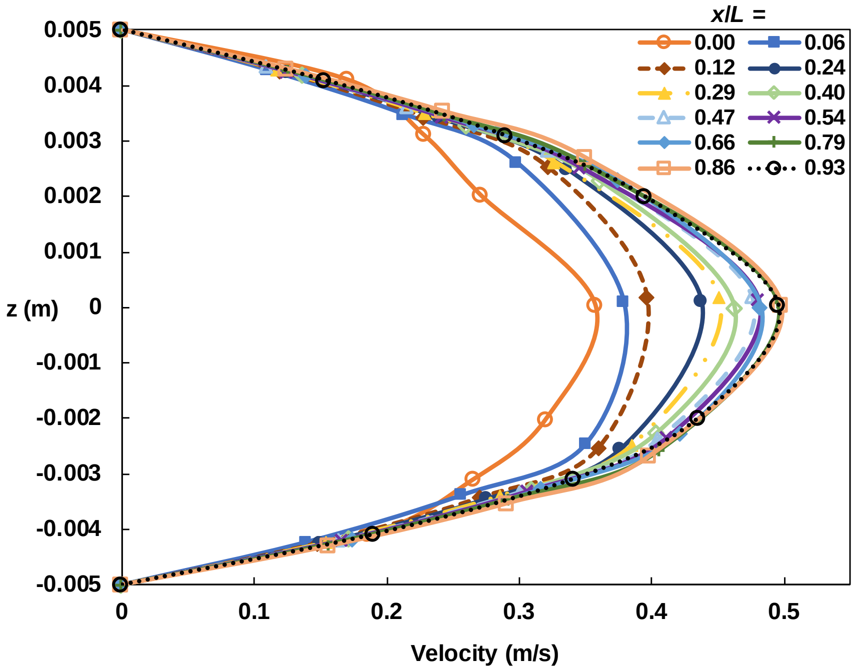

Fig. 8. Profiles of streamwise velocity, U_x, along the channel centerline for heater input = 100 W (ΔT ≈ 200 °C) and a flowrate of 10 SLM.

Figure 9 shows the simulation temperature results for ΔT ≈ 200 °C for both flowrates at the mid-width of the channel and at the mid-height of the channel. The temperatures of the solid aluminum walls are also shown, but are uniform on this temperature scale. As expected, the flow temperature varies significantly across the height of the channel from T_{cold} at the cold wall to T_{hot} at the heated wall. The temperature distributions do not vary significantly across the width of the channel, although there are temperature variations at the beginning of the channel as the thermal profiles develop. The 3 SLM case reaches a thermally fully developed state before the 10 SLM case, which is consistent with the trend for velocity development. The 3 SLM case also has a slightly warmer fully developed flow temperature at mid-height compared to the 10 SLM case, which is consistent with the warmer T_{hot} for 3 SLM.

The centerline temperature profiles given in Fig. 10 illustrate the thermal development of the 10 SLM flow with an inlet flow temperature of 50 °C. The channel inlet profile (x/L = 0) is flat across much of the channel height, with sharp gradients in temperature near the hot and cold walls. Downstream of the inlet, the profile gradually becomes more linear. By x/L = 0.47, the profile is close to linear and within 5 % from the profile at the end of the channel. Therefore, the flow is thermally fully developed with a linear temperature profile by the second half of the channel for the case of 10 SLM. For 3 SLM, the flow is thermally developed by x/L = 0.2. The top and bottom surface temperatures are relatively uniform for all locations along the length of the channel, as expected from the uniformity of the T_{hot} and T_{cold} results from Figs. 4 and 6. The slope of the fully developed profiles defines the temperature gradient experienced by aerosol soot particles to drive thermophoretic motion. The temperature gradients in Fig. 10 are close to 200 °C/cm, which is roughly the temperature difference divided by the channel height, ΔT/(1 cm).

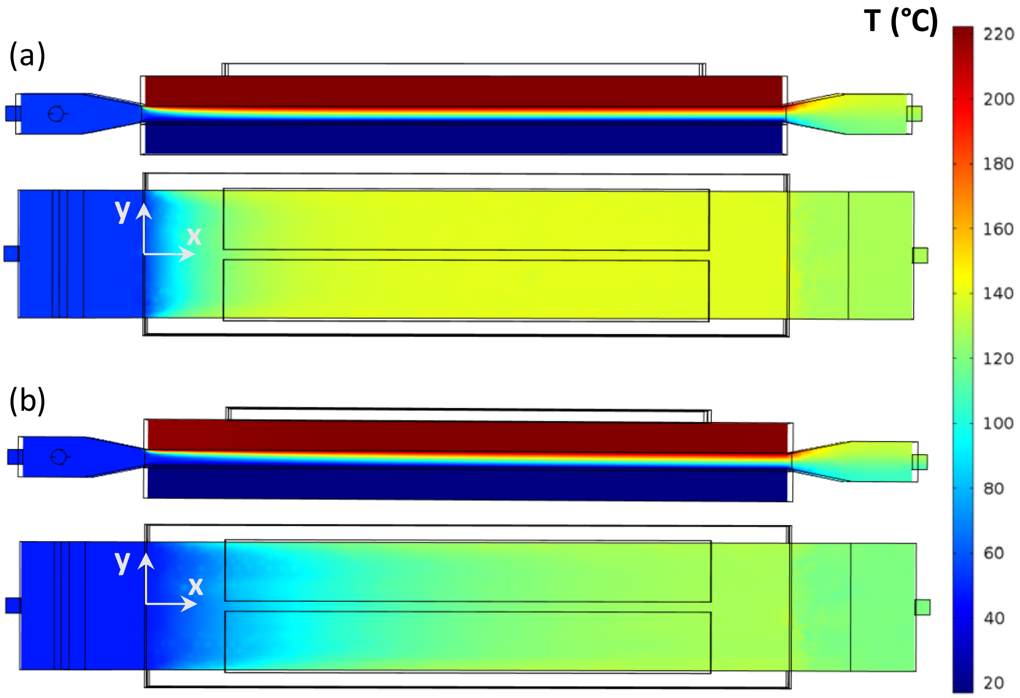

Fig. 9. Flow temperatures at the mid-height of the channel and the mid-width of the channel for heater input = 100 W (ΔT ≈ 200 °C) and flowrates of (a) 3 SLM, and (b) 10 SLM.

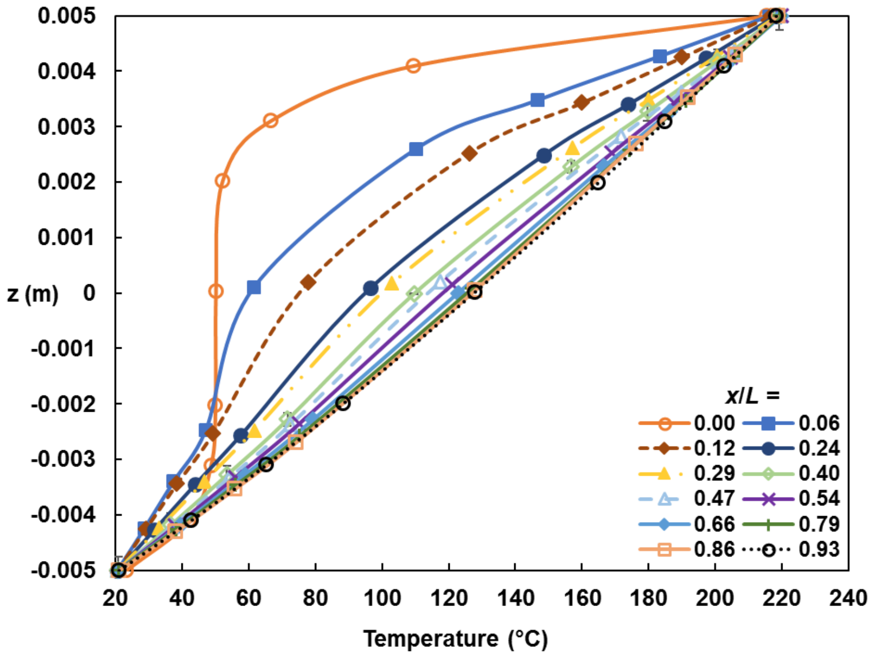

Fig. 10. Temperature profiles along the channel centerline for heater input = 100 W (ΔT ≈ 200 °C) and a flowrate of 10 SLM.

2.4 Soot Deposition Modeling

To model the soot deposition, flow and heat transfer simulations were also run in FDS to predict soot deposition within the channel. The FDS simulations were transient in order to track the buildup of soot on the sensor surface. As previously mentioned, FDS has aerosol deposition models for thermophoresis, gravitational settling and combined diffusion-turbulent transport that can be turned on or off in the simulation [12]. Additionally, the aerosol models treat soot as an additional gaseous species whose motion is dominated by the convective flow of the surrounding fluid. To account for the thermophoretic, gravitational or diffusion-turbulent transport to surfaces, an additional velocity is applied to the aerosol species based on empirical relationships to the driving parameters. In grid cells adjacent to surfaces, the thermophoretic deposition velocity is determined for soot using Eq. (1) and correlations for K_{th} [9]. FDS uses the temperature in the first grid cell above the wall for T_p and the other temperature dependent properties needed to calculate K_{th} and v_{th}. The thermophoretic mechanism was activated in all of the simulations, and the gravitational mechanism was activated for horizontally oriented cases only. Initial studies showed that the turbulent deposition mechanism did not contribute noticeably to the results for this laminar simulation and therefore remained off in the FDS simulations.

Because of the limitations associated with meshing non-rectangular geometries in FDS, the domain was limited to the rectangular channel only, excluding the inlet or outlet plenums. Additionally, FDS only calculates solid heat conduction in one direction, so heat transfer within the solid aluminum walls was not included. The computational mesh was a structured rectangular grid with spacing of 5 mm across the length (x-direction) and width (y-direction), and 1 mm across the height (z-direction). The simulations were run for 1000 s, with steady-state reached by 10 s (deposition rate was less than 0.5% of final value).

Constant temperature boundary conditions were applied directly to the hot and cold surfaces of the channel because the full CFD simulations found that the temperature variation across the hot and cold surfaces of the channel were minimal. For the cases of $\Delta T = 200$ °C, the hot and cold surface temperatures were set to 221 °C and 21 °C, respectively. For the cases of $\Delta T = 100$ °C, the hot and cold surface temperatures were set to 115 °C and 15 °C, respectively. As in the full CFD simulations, the side wall boundary conditions were set to adiabatic. For the inlet boundary condition, the velocity profiles in the y- and z-directions were specified based on the full CFD solution. In the z-direction, the velocity profile was defined for ten interior points spaced by 1 mm and set to zero at the walls. In the y-direction, the velocity profile was defined for 16 interior points spaced by 5 mm and set to zero at the walls. A variation in temperature profile was not possible in FDS, so a uniform inlet temperature was applied corresponding to the measured flow inlet temperature in Table 1. The inlet mass flowrate calculated by FDS was within 2% of the mass flowrate in the full CFD simulation. The temperature outside the flow outlet, was set to the measured flow outlet temperature in Table 1.

The domain of the channel in FDS is shown in Fig. 11 along with the inlet velocity boundary condition and a slice of the steady-state streamwise velocity, U_x, along the channel centerline for the case of 3 SLM and $\Delta T = 200$ °C. The channel velocity profile appears similar to the laminar profile found in the full CFD solution, but with a higher peak velocity. The peak velocity is close to 0.2 m/s in FDS, compared to 0.15 m/s in the full CFD simulation. The peak also is shifted slightly toward the cold side rather than being located at mid-height.

The temperature boundary conditions and steady-state temperatures for the same condition are shown in Fig. 12. The uniform temperatures at the inlet and cold side arise from the temperature boundary conditions. Also shown are the temperatures for the adiabatic side wall and the centerline plane, which are very similar to each other. Like the full CFD simulation, the temperature profile appears to become linear after some development length. However, the temperature gradient is less than the expected gradient of 200 °C/cm. This is possible because the gradients between the walls and the cells closest to the walls are steeper than the gradient in the interior flow, which is similar to the behavior of the thermal profile for a turbulent boundary layer, rather than a linear thermal profile expected for fully developed laminar channel flow. This has an effect on the thermophoretic velocity calculated by FDS. FDS calculates the temperature gradient from the wall heat flux divided by the air thermal conductivity. For the case of 3 SLM and $\Delta T = 200$ °C, the calculated ∇T in the fully-developed half of the channel is 119 °C/cm, while the expected ∇T is 200 °C/cm. For 3 SLM and $\Delta T = 100$ °C, the calculated ∇T in the fully-developed half of the channel is 54 °C/cm, while the expected ∇T is 100 °C/cm.

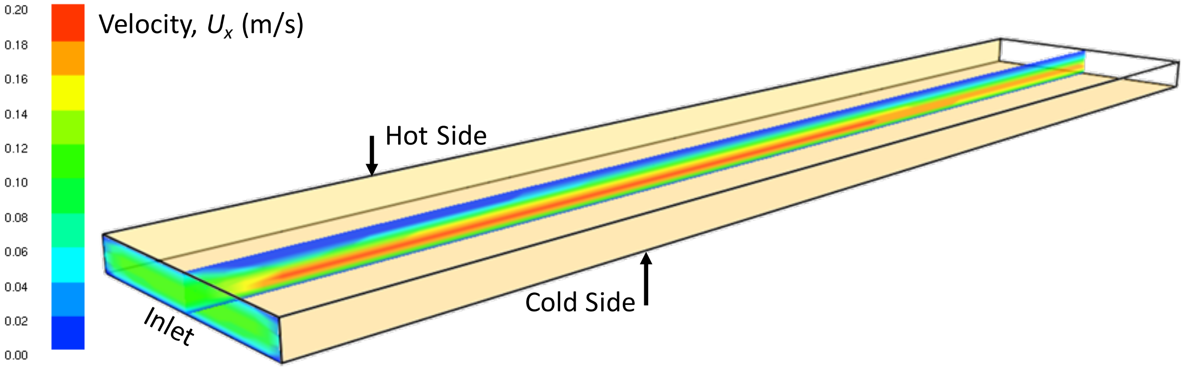

Fig. 11. Domain of channel modeled in FDS with contours of streamwise velocity for the flowrate of 3 SLM and $\Delta T = 200$ °C.

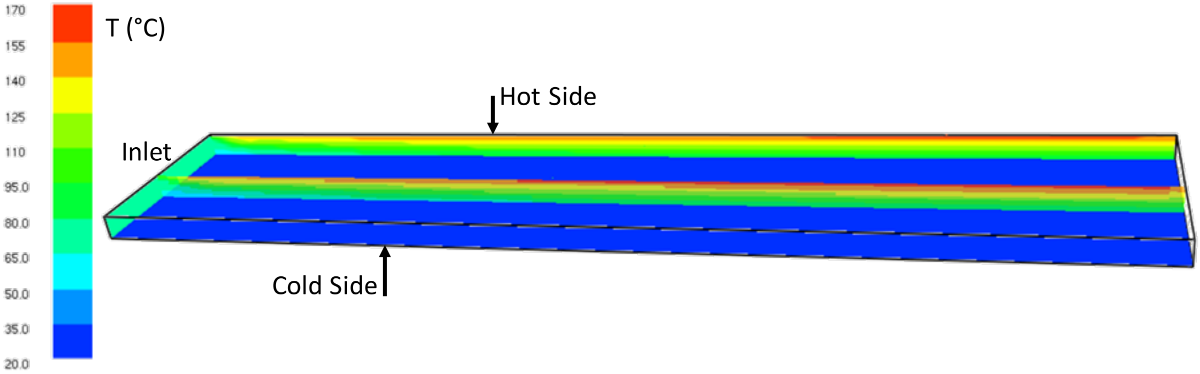

Fig. 12. FDS temperature contours at the channel inlet, cold surface, channel centerline and adiabatic side wall for $\Delta T = 200$ °C and the flowrate of 3 SLM.

Soot was introduced as part of the inlet flow, and the distribution of surface deposition and thermophoretic deposition velocity, v_{th}, were monitored. The inlet soot concentration was set to 67 mg/m^3, although this value did not affect v_{th} or the distribution of soot deposition, only the amount of deposit. The default soot properties were used, which were the molecular weight of 12.0107 g/mol, solid density of 1800 kg/m^2, σ (Lennard-Jones hard-sphere diameter) of 3.798 Å, ε/k (Lennard-Jones attractive energy well/Boltzmann constant) of 71.4 K, and thermal conductivity of 0.26 W/m-K [12]. The soot mean diameter parameter was constant within a simulation, three different diameters were considered: 0.035 µm, 0.121 µm and 1.47 µm to cover a range of expected particle sizes.

Initial deposition simulations in FDS were run at various conditions similar to the experiments to determine general trends. First, after reaching steady-state, v_{th} remained constant and did not change for the rest of the simulation. Second, halving the inlet soot concentration approximately halved the rates of deposition. Finally, when gravitational deposition was included for horizontal simulations, the deposition rate increased by approximately 17 % for a temperature difference of 200 °C.

The final deposition simulations comparing the three different particle sizes were completed for the cases of 3 SLM and both temperature differences of 200 °C and 100 °C. Fig. 13 shows the results of deposition mass loading at 15 min (900 s) into the simulation. The mass loading increases in the upstream portion of the channel, but then is relatively even across most of the downstream portion of the channel. The FDS calculated deposition velocity, v_{FDS} also increases along the length as the flow and temperature profiles develop. The value of v_{FDS} covering the largest area in the downstream portion of the channel is determined for these six cases and given in Table 2. As the particle size increases, v_{FDS} and the amount of deposition decreases, but the distribution remains similar.

Table 2. Steady-State v_{FDS} in Downstream Half of Channel

	Particle diameter, D_p		
ΔT	**0.035 µm**	**0.121 µm**	**1.47 µm**
200 °C	0.41 mm/s	0.39 mm/s	0.29 mm/s
100 °C	0.17 mm/s	0.16 mm/s	0.12 mm/s

When the temperature difference is doubled from 100 °C to 200 °C, the amount of deposition increases (note the change in scale between Fig. 13a and 13b). The increase is slightly more than double for all particle sizes (about a factor of 2.2). Comparing the deposition velocities, the temperature difference also has a slightly greater than doubling effect for all particle sizes (about a factor of 2.4).

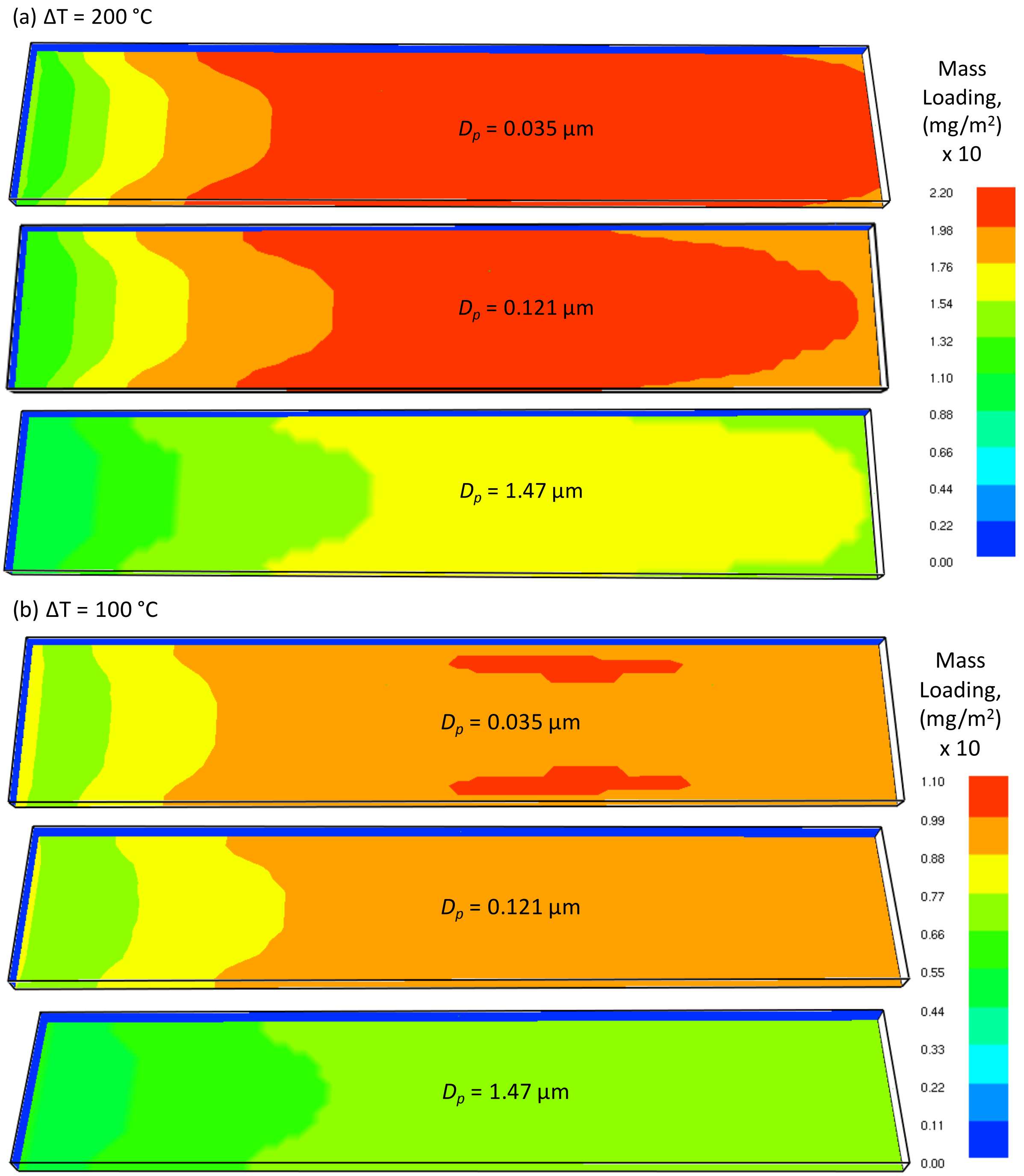

Fig. 13. Mass loading of soot deposition as predicted by FDS at 900 s for the cases of 3 SLM and (a) ΔT = 200 °C and (b) ΔT = 100 °C for three different particle sizes, D_p.

3. Soot Deposition Measurements

A laminar diffusion flame burner was used to generate soot for deposition. Propene fuel exited a 1.0 cm diameter tube surrounded by co-flowing air from a 12.0 cm diameter ceramic honeycomb, enclosed by a brass chimney. After a tripper plate to induce mixing of the soot, dilution air was injected into the upper stage of the burner. All fuel and air flows to the burner were set by mass flow controllers. The flowrates were 0.055 SLM for the fuel, 54.08 SLM for the co-flow air, and 32.47 SLM for the dilution air. Additional experiments at 0.077 SLM were also completed in order to calculate deposition velocity only. The burner operated at a slight positive pressure of approximately 1.5 kPa to allow a portion of the flow exiting the burner to be directed to the channel for deposition. The channel dimensions, flow and temperature conditions are described in detail in Sec. 2.2. The total duration of deposition was typically 60 min, although one test was 40 min.

The incoming soot aerosol concentration, C_p, entering the channel was measured by two methods, by flowing part of the exhaust from the burner through a tapered element oscillating microbalance (TEOM), and by flowing part of the exhaust through a filter to measure the change in mass captured at the measured flowrate. For the latter method, both the change in mass on the filter and the flowrate were required to calculate the concentration. The average for each flowrate and measurement method and the expanded uncertainties (μ) of C_p are given in Table 3. The concentrations are given for the mass of soot in air at standard conditions (101 kPa and 21 °C). In some cases, the statistical variation between the $C_{p,avg}$ in repeated experiments was greater than the statistical variation of C_p within individual experiments. Therefore, both the overall uncertainty for a certain condition (for $C_{p,avg}$) as well as the average uncertainty within experiments at that condition (Exp. C_p) are reported. The uncertainties are derived from the standard deviation of the measurements multiplied by a coverage factor. For the uncertainty in $C_{p,avg}$, the coverage factor is the *t*-value for a 95 % confidence interval. For the Exp. C_p, the coverage factor is 2 for a 95 % confidence interval. The soot concentration is greater when the fuel flowrate is higher as expected. Comparing the two types of measurements, the direct filter measured greater soot concentration than the TEOM, but the two-sample *t*-test for equal means [13] was used to determine if the differences were statistically significant. For the 0.055 SLM flowrate, the TEOM and filter measurements are the statistically equivalent (95 % confidence), but for 0.077 SLM the measurements are not statistically equivalent. When both concentration measurements are available, the more direct filter measurement is used to calculate deposition velocity.

Table 3. Particle Concentration Measurements and Uncertainty

Propene Flow (SLM)	$C_{p,avg}$ (mg/m^3) at 101 kPa, 21 °C	**No. of Exp.**	**Std. Dev.** of $C_{p,avg}$ (mg/m^3)	**Coverage Factor** of $C_{p,avg}$	**μ** of $C_{p,avg}$ (mg/m^3)	**Std. Dev.** of Exp. C_p (mg/m^3)	**Coverage Factor** of Exp. C_p	**μ** of Exp. C_p (mg/m^3)
0.055	TEOM 70	22	10.0	2.080	± 20.8	3.1	2	± 6.2
	Filter 70	15	2.5	2.145	± 5.4	3.8	2	± 7.6
0.077	TEOM 108	3	2.4	4.303	± 10.4	19.9	2	± 39.8
	Filter 125	11	8.6	2.228	± 19.2	5.8	2	± 11.6

The deposition target boards were along the cold side of the channel to measure the soot deposition during and after a test. The deposition target boards were standard circuit boards (IPC B-24) with parallel traces in an interdigitated comb pattern. The board dimensions were

10.2 cm long by 11.4 cm wide. As shown in Fig. 3, each board had four separate interdigitated comb pattern traces, and the channel fit four test boards along its length. The comb patterns were aligned perpendicular to the flow, and the circuit terminals were accessible outside of the channel when fully assembled. The copper traces in the comb patterns were 0.40 mm wide with 50 mm gaps between adjacent traces. The total circuit length of each comb pattern was 518.2 mm. The deposition area, the area just between the interdigitated pattern, was 31.5 mm by 16 mm, or 504 mm^2. The surface insulation resistance for comb patterns without deposition was 10^9 to 10^{12} ohms.

Periodically during the deposition and afterwards, the current of each comb pattern was measured with a pico-ammeter and an applied voltage of 5 V DC. Individual current measurements were recorded once every 3 s to 4 s and cycled through the comb patterns in about 50 s. When the current was not being measured, the DC voltage was removed to minimize any deposition due to possible electrical charge present on the soot particles. The final current was measured directly after the exposure and then again once the channel had been disassembled and the surfaces had come to room temperature to verify the final current measurement. In initial tests, intermediate current measurements were taken during the deposition exposure for 2 min at a time. In later tests, the soot exposure was paused before any intermediate current measurements were taken to eliminate any possibility of electrically driven deposition. Additionally the current measurement could be taken for a longer period of time during a pause in the soot exposure, to obtain a more reliable average measurement.

A comparison of the time-resolved raw current measurements for the same comb pattern in three experiments with nominally the same conditions is given in Fig. 14. The data shown are for a single comb on board #2 (3rd from the inlet), 0.055 SLM fuel flow, 3 SLM flow through the channel, $\Delta T = 200$ °C, and the vertical orientation. The standard deviations over the means for the experiments at 30 min exposure are 0.14 for three data points from test 1E, 0.06 for the ten points from test 1A, and 0.03 for the ten points from test 1B. When the data was recorded for a longer period of time, the measurement could reach a steady value and the uncertainty was reduced.

After the soot deposition was completed, the target boards were removed from the channel to measure the mass of deposited soot. Two methods, to be discussed in the following two sections, were used: direct gravimetric measurement and mass correlation to the light transmission through a suspension of the soot in water and soap. Because the methods determined the mass of soot deposition on different size areas, the mass was converted to a mass loading by dividing by the area of deposition. Then the soot mass loading was compared to the final conductance, *G*, calculated from the measured current and applied voltage.

$$G = 1/R = I/V \tag{3}$$

The intermediate soot mass loading amounts were calculated by scaling the final mass loading by the intermediate exposure time relative to the total exposure time. This scaling assumed that the deposition rate was constant in time, which was assumed valid because the flow and temperatures were steady during the exposure. The expanded uncertainties in *G* were calculated based on the standard deviation of the current measurements and a coverage factor of 2. These uncertainties varied between experiments and are shown as error bars the plots in Sec. 4.2.

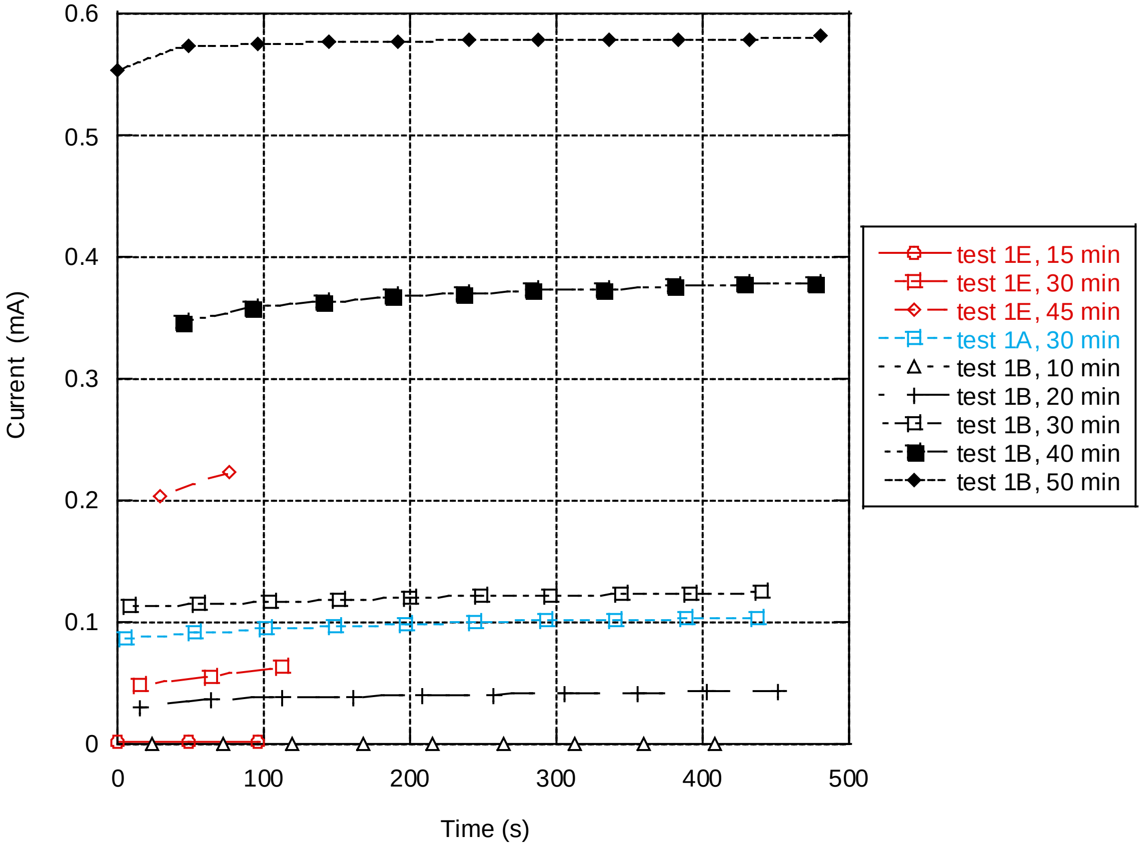

Fig. 14. Raw current measurements at various intermediate times of the soot exposure for a single comb on the second board in three experiments with 0.055 SLM fuel flow, 3 SLM flow in channel, ΔT of 200 °C, and vertical orientation.

3.1 Gravimetric Measurement Method

The most direct method to measure the amount of deposited soot was to measure the change in mass of the substrate surface. Prior to deposition, a lightweight circular piece of aluminum foil was taped to the center of the target board flush with the surface. The mass of the foil circle was measured before and after the deposition. The measurement of mass deposit on the foil ranged from 0.05 mg to 0.23 mg with an uncertainty of ± 0.0014 mg based on the precision of the mass balance. The area of deposition was found by subtracting the areas covered by tape from the total area of the foil circle, which had a diameter of 47 mm. Photo analysis revealed that about 2 % of the foil area was covered by tape. Example photos of the foil circle taped to board #3 are shown in Fig. 15 for a deposition experiment with 0.055 SLM fuel flow, 3 SLM flow through the channel, ΔT of 200°C, and the vertical orientation. Uncertainties in the deposit area were estimated to be ~ 10^{-5} using the standard deviation of the deposit areas from different foil circles. The uncertainty in area contributed less than the uncertainty in mass to the combined uncertainty of soot mass loading. The combined expanded uncertainty in gravimetric measured soot mass loading was found to be ± 1 mg/m^2. Because the foil and tape blocked soot from depositing on part of the copper traces, the current leakage could not be measured during the deposition exposures that used the foil, but the current was obtained from deposition exposures that used the light transmission method to measure soot mass loading.

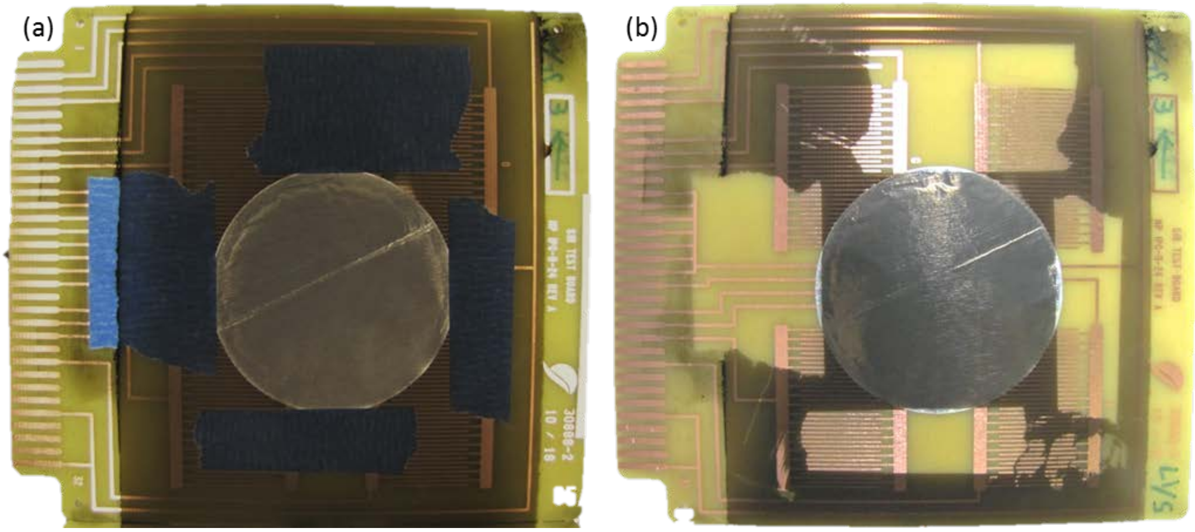

Fig. 15. Photographs of deposition on the foil circle taped to board 3 for 0.055 SLM fuel flow, 3 SLM flow in channel, ΔT of 200 °C, vertical orientation, (a) before and (b) after tape removal.

3.2 Light Transmission Method

The second method to measure the deposited soot does not involve attaching anything to the deposition target board, so the conductance could be measured and directly compared to the soot mass loadings. As described below, the soot was removed from the surface of the boards and mixed in a suspension with water and soap to help the soot remain in a more uniform suspension. The light transmission through the suspension was correlated to the mass of soot in the sample using calibration mixtures. A similar method was employed by Dillner et al. [13] who measured the light transmission of atmospheric elemental carbon particles in isopropyl alcohol/water mixtures to derive the mass extinction efficiency of the samples.

Figure 16 shows the steps involved in determining the mass loading of soot deposited on each comb pattern on the target boards. Figure 16a shows the board after disassembly of the channel. The soot appeared uniformly distributed across the board independent of flow direction, which is from left to right. Before removing the soot, tape was placed on the boards surrounding the area outside the interdigitated copper traces (Fig. 16b). A small piece of optical tissue was wetted with isopropyl alcohol and used to remove the soot from the board as shown in Fig. 16c. The pieces of tissue containing soot from one comb pattern were placed in a glass bottle with 12 mL of distilled water containing 0.5 mg/mL of powdered soap (Fig. 16d). The bottle was shaken by hand and sonicated for at least 30 min or until as much soot as possible had been released from the tissue (Fig. 16e). Three milliliters of the liquid were removed from the bottle into a cuvette for the transmission measurement. Figure 16f shows that the liquid was still transparent, but slightly darkened from the white background in the image. Bubbles were removed by sonicating the cuvette for a few seconds.

The cuvettes were loaded into a spectrophotometer to measure the light transmission at a wavelength of 400 nm. The spectrophotometer performed an internal wavelength calibration each time it was turned on. Just before measuring the transmission of soot samples, the spectrophotometer was zeroed (set to 100 % transmission) for a blank cuvette with distilled water and soap. The process of zeroing and measuring the transmissions was repeated three times to obtain three transmission measurements for each soot sample.

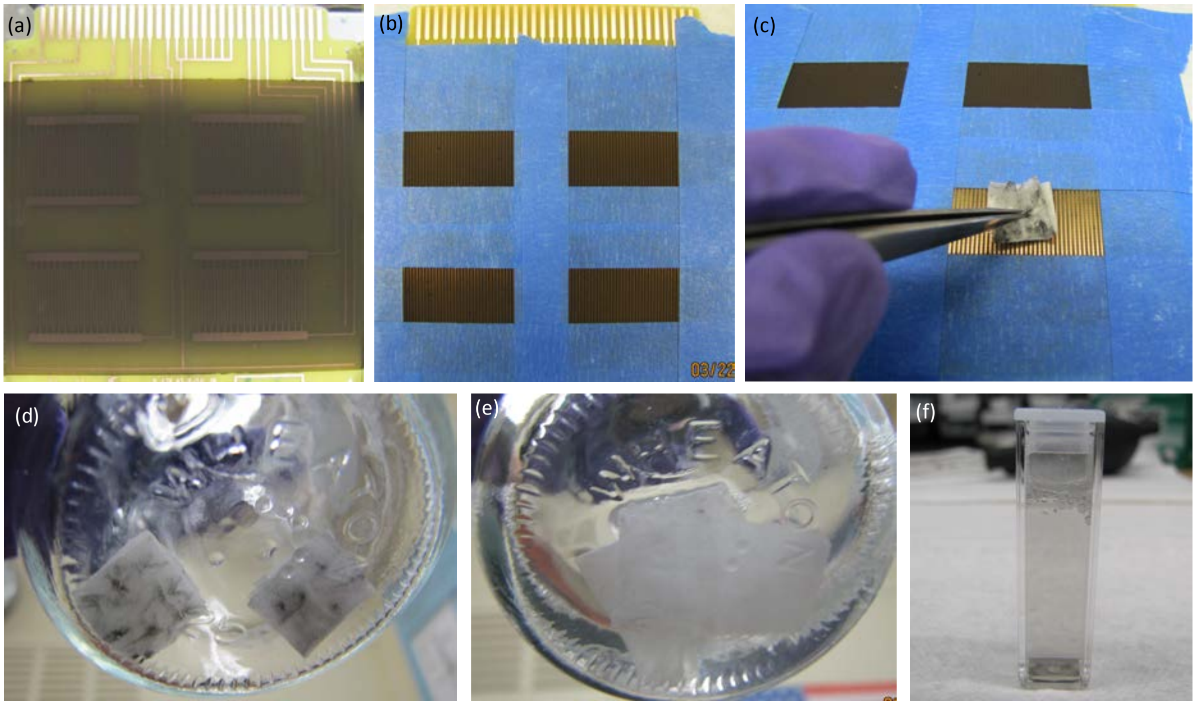

Fig. 16. Process for removing soot from target surface and suspending in water/soap mixtures. Images are (a) board after deposition, (b) tape surrounding interdigitated copper traces, (c) removing soot using tissue soaked with isopropyl alcohol, (d) used tissues in a bottle with distilled water and soap solution, (e) tissues after shaking and sonicating, and (f) soot sample in cuvette to measure transmission.

The light transmission was related to the soot concentration by a calibration determined from multiple samples with varying but known concentrations of soot. About 5 mg of propene soot was measured by a mass balance (± 1 µg) and mixed with 100 mL of a distilled water and powdered soap "working solution" (soap concentration 1 mg/mL) to generate a "soot base". The soot base was diluted by 50 % by volume with distilled water, resulting in the calibration mixture with 28.2 µg soot/mL, called C50. A calibration mixture with 30 % by volume soot base, 20 % by volume working solution, and 50 % by volume distilled water resulted in a calibration mixture with 16.9 µg soot/mL, called C30. The weakest calibration mixture, called C10, was made with 10 % by volume soot base, 40 % by volume working solution, and 50 % by volume distilled water, with 5.6 µg soot/mL. The soot concentrations for the calibration mixtures had a combined expanded uncertainty of ± 2 %.

The calibration mixtures had transmission levels, τ, ranging from 4 % to 50 % as shown in Fig. 17. The uncertainty in τ (vertical error bars) was statistically determined from multiple readings on different days to account for sample variation in time and variations in the spectrophotometer readings. The transmission measurement expanded uncertainty ranged from ± 0.2 % transmission for C50 to ± 1.6 % transmission for C10. The uncertainty in τ was generally smaller for the mixtures with lower transmission readings and higher soot concentrations, and larger for the mixtures with higher transmission readings and lower soot concentrations.

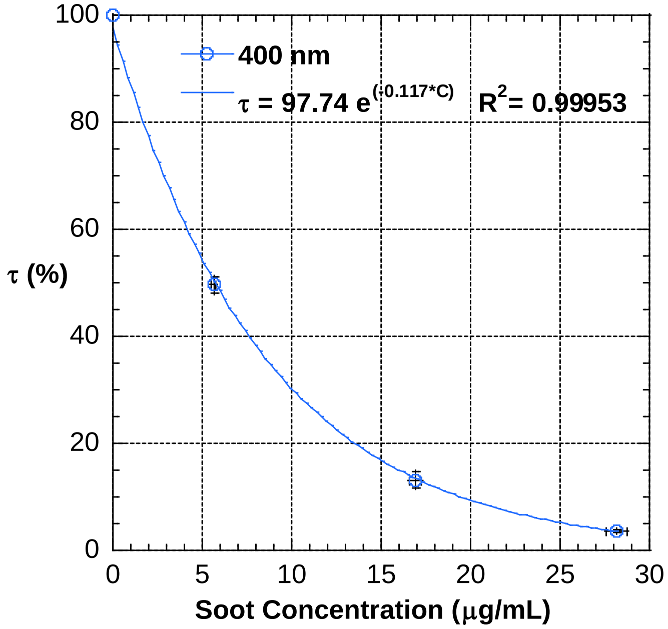

Fig. 17. Calibration data and exponential fit line of transmittance versus soot concentration at 400 nm. Error bars are shown for a 95 % confidence level.

The calibration curve was defined by fitting an exponential curve to the measured data and the intersection of 100% transmission for zero soot concentration in Fig. 17. The exponential fit was inverted to give the soot concentration in terms of the transmission measurement in Eq. (4), where the units are given in brackets.

$$C[\mu\text{g/mL}] = -8.55[\mu\text{g/mL}]\ \ln(\tau[\%]/97.74) \quad (4)$$

The soot mass loading was calculated by multiplying the soot concentration by the volume of solution and dividing by the deposition area (504 mm^2). Considering the uncertainty contributions from the transmission measurement, the calibration curve, the volume measurement, and the area measurement, the combined uncertainty in soot mass loading by transmission was ± 10 mg/m^2, which was 10 % to 15 % of the typical soot loading value.

While taking transmission measurements, it was observed that paper fibers from the tissue were present in the cuvettes and were settling to the bottom after a couple of hours. As the transmission readings were repeated, the soot mass loadings dropped significantly as shown by the data points for five samples in Fig. 18a. Figure 18a plots the mass loading versus the time after the mixture was sonicated. The drop in loadings was due to settling of both the paper fibers as well as the smaller soot particles. Because the paper fibers were larger than the soot particles, it could be assumed that the fibers settle out quicker than soot.

The rate of decrease in the soot loading due to settling of only soot particles could be determined by repeated transmission measurements of the calibration mixtures without re-sonicating. The calibration mixtures were made without using any tissue, and so did not contain any paper fibers. An equivalent soot mass loading of the calibration mixtures was calculated using Eq. (4) using the measured soot concentration, 12 mL for solution volume, and 504 mm^2 for deposit area. Based on extensive measurements of nine different calibration mixtures, the loadings were found to decrease linearly with time. However, the rate of decrease varied depending on the initial soot loading as plotted in Fig. 18b. The best fit trendline to the rate of decrease versus initial soot mass loading was in the form of a power relationship. The power fit allowed calculation of predicted linear rates of change in soot mass loading due to soot particle settling only for the test samples with paper fibers. The straight lines in Fig. 18a show the linear decrease in soot loading due to only soot particle settling, based on the predicted rate of decrease determined from the fit in Fig. 18b. The predicted linear decrease lines were recalculated after each transmission measurement was made to determine if the measured loading was decreasing faster (paper fibers still in suspension) or at the same rate as predicted (only soot remains in suspension). Transmission measurements were continued until the predicted line overlapped with two consecutive measurements, indicating the paper fibers had settled to the bottom of the cuvette and the soot mass loading was decreasing only due to soot particle settling. The intersection of the predicted loading with t = 0 min was used as the value of soot mass loading found by measuring light transmission.

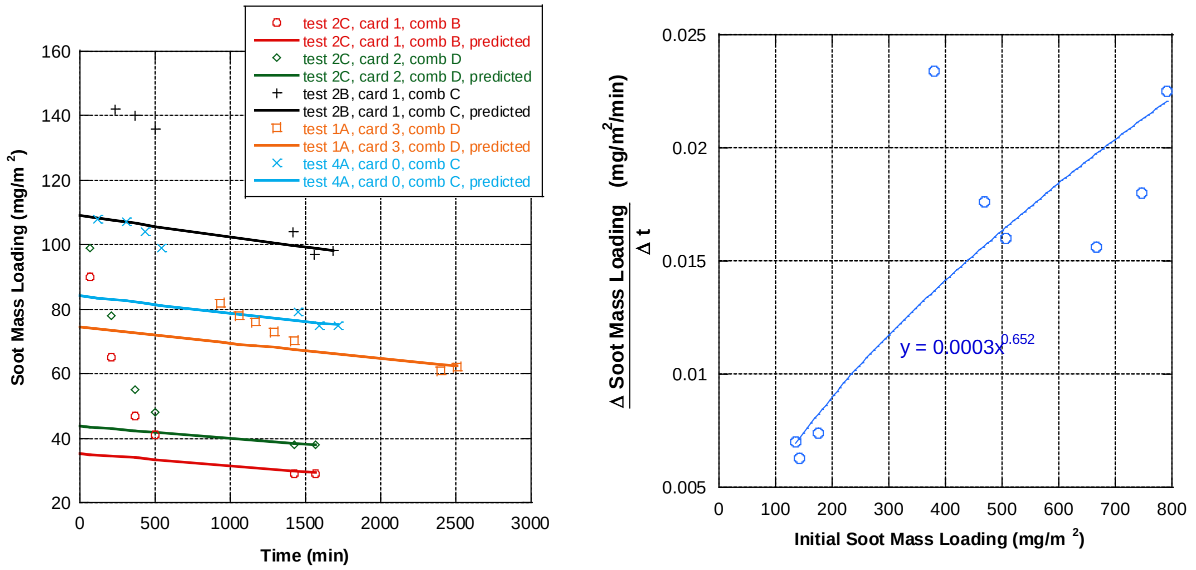

Fig. 18. Soot and fiber settling analysis: (a) Points show transmission based soot mass loading measurements decreasing in time, and solid lines show predicted decrease of the soot mass loading due to the settling of only soot particles. (b) Points show rates of change in soot mass loading of calibration mixtures as a function of initial soot mass loading, and the corresponding power fit line.

4. Results and Discussion

4.1 Deposition Results

The effects of channel flowrate, channel orientation and temperature difference were each varied between two conditions in the deposition experiments. Figure 19 shows a photo of the deposition surface after 60 min of exposure for each of the conditions tested and the specific experiment pictured. Figs. 20 and 21 plot the final conductance (in black) and gravimetric soot mass loading (in red) at 60 min as a function of distance from the channel inlet to the center of the measurement location. Figure 20 compares the effects of orientation for 3 SLM on the left and 10 SLM on the right. Figure 21 compares the effect of temperature gradient for 3 SLM on the left and 10 SLM on the right. All of the experiments are included in Figs. 20 and 21 except the tests that continued the soot exposure during the intermediate current measurements. Repeat experiments for most conditions show the reproducibility of repeated tests. The conductance points (in black) are an average of the measurements for the two adjacent comb patterns, while the gravimetric soot mass loading points (in red) are for a single target placed at center of each target board.

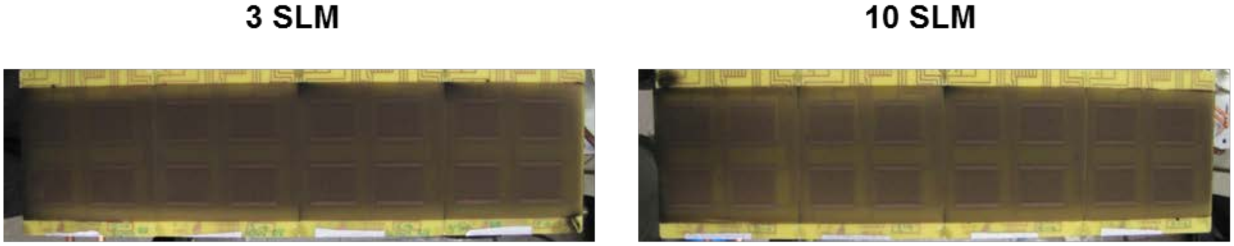

ΔT = 200°C, Vertical (Test 1B)   ΔT = 200°C, Vertical (Test 4A)

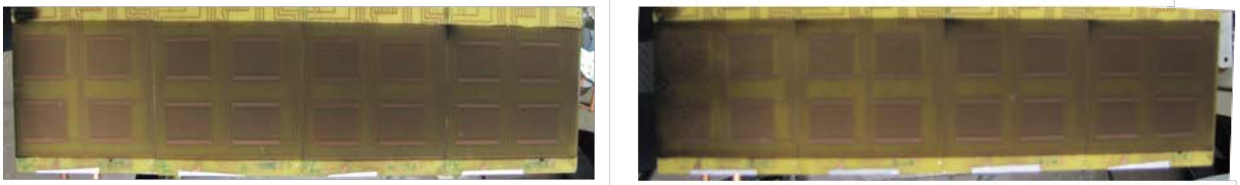

ΔT = 200°C, Horizontal (Test 2B)   ΔT = 200°C, Horizontal (Test 5A)

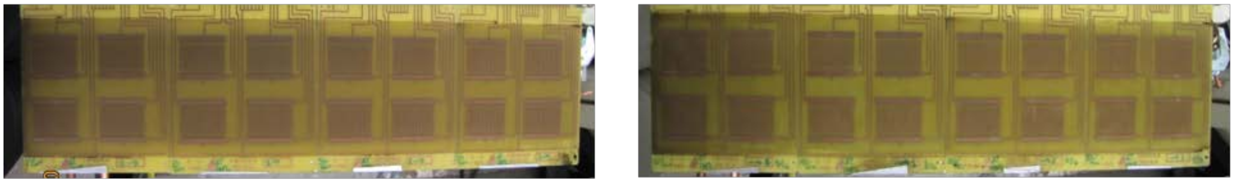

ΔT = 100°C, Vertical (Test 3A)   ΔT = 100°C, Vertical (Test 6A)

Fig. 19. Photos of soot deposition for each of the conditions tested, with flow from left to right.

Comparing the deposition photos between the two flowrates in first row of Fig. 19, it is difficult to see any differences. However, there are slight differences in the spatial distributions of *G* (open black symbols) between the two flowrates in Fig. 20a and b for the vertical orientation. For 3 SLM, *G* initially increases, stays relatively flat and then begins decreasing. For 10 SLM, *G* increases more slowly and then levels off in the second half of the channel with only a slight decrease towards the outlet. The gravimetric mass loading measurements show similar qualitative trends: for 3 SLM in Fig. 20a the mass loading is flat and then decreases, and for 10 SLM in Fig. 20b the mass loading increases and then becomes flat. These differences are likely due to differences in the point where fully developed flow and temperature profiles are achieved. The 10 SLM flow case becomes fully developed about halfway through the channel, while the 3 SLM flow and temperature profiles become fully developed earlier in the channel.

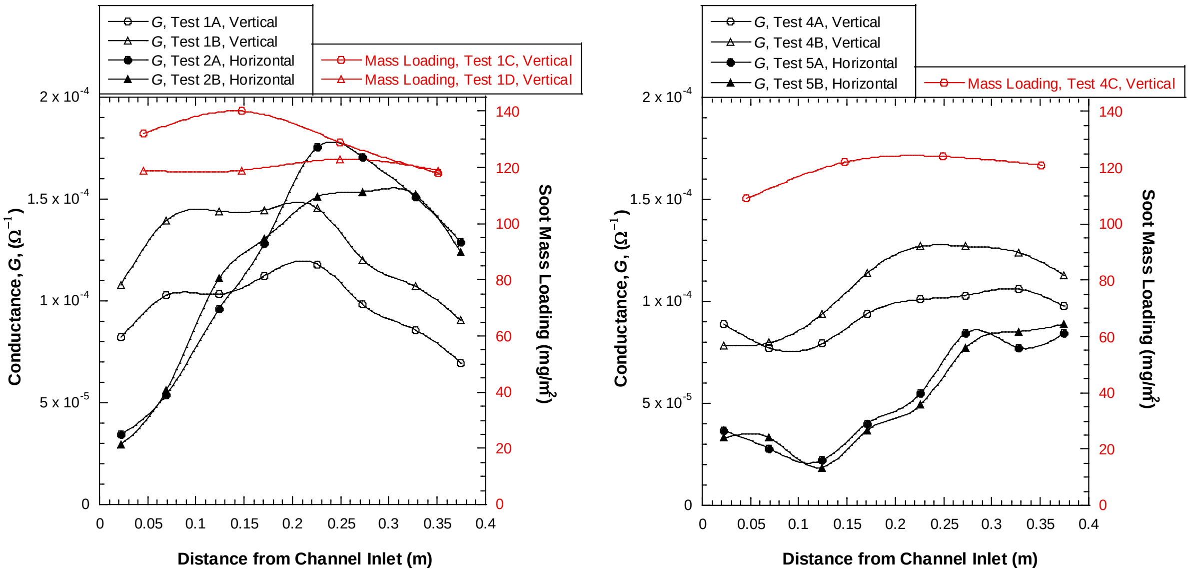

Fig. 20. Final sensor conductance and gravimetric soot mass loading as a function of distance for ΔT = 200 °C at both vertical and horizontal conditions for (a) 3 SLM and (b) 10 SLM.

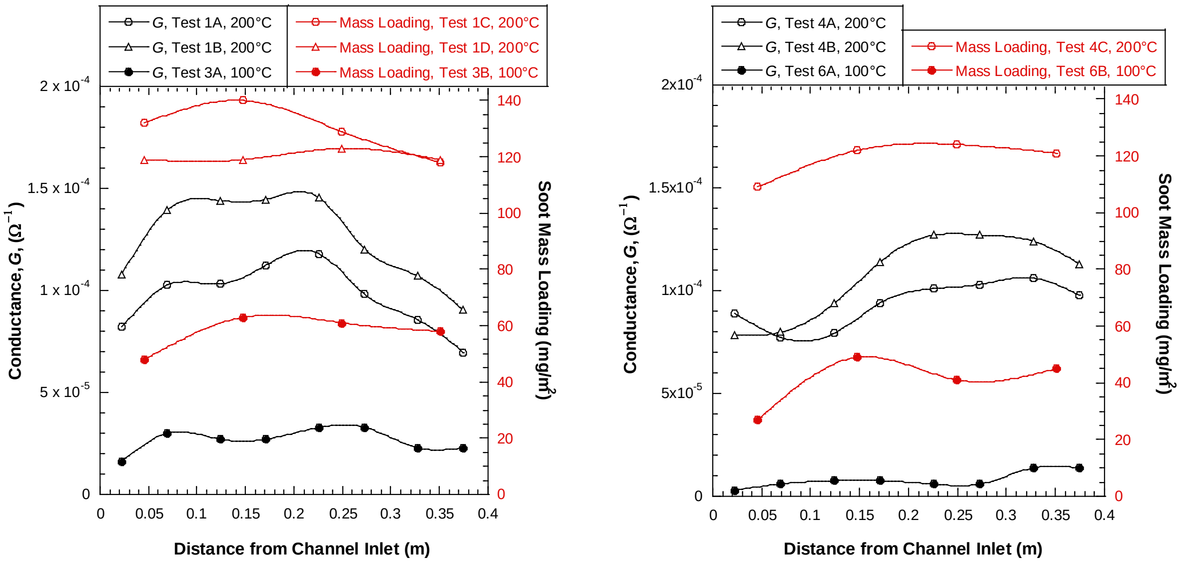

Fig. 21. Final conductance and gravimetric soot mass loading as a function of distance for vertical orientation at both ΔT = 200 °C and 100 °C for (a) 3 SLM and (b) 10 SLM.

Differences in spatial distribution are also observed between vertical and horizontal orientations. Comparing the vertical and horizontal deposition photos in Fig. 19, the deposition appears thinner on the boards closest to the inlet for the horizontal orientation, especially for 3 SLM. The quantitative *G* measurements in Fig. 20a also show a large increase along the channel for horizontal (filled black symbols) compared to the more gradual increase for vertical (open black symbols). As shown in Table 1, the inlet temperature for vertical orientation is higher than for horizontal orientation, leading to earlier development of the linear temperature profile across the thickness of the vertical channel. Before the temperature profile becomes linear, the thermophoretic driving mechanism is weaker across most of the channel height because of the flatter temperature gradient, as shown in Fig. 10. Although the vertical experiments have more uniform deposition across the boards, the agreement between repeat experiments in Fig. 20 indicates that vertical experiments may be less reproducible than horizontal because variations in external buoyant flow play a role in upstream heating in the vertical configuration.

The effect of temperature difference can be observed by comparing ΔT = 200 °C in the top row of deposition photos and ΔT = 100 °C in the bottom row of Fig. 19. The temperature gradient is expected to directly affect the amount of soot deposition according to Eq. (1) for v_{th}. From the images, it is clear there is less deposition for the smaller temperature difference. Figure 21 also shows that *G* and soot mass loading are approximately cut in half when the temperature difference is reduced by half. The spatial distributions are similar between cases of ΔT = 200 °C and ΔT = 100 °C, with less variation observed for the smaller temperature gradient when comparing *G*. Overall, it appears the effect of temperature gradient is felt uniformly across the channel.

4.2 Mass and Conductance Correlation

The relationship between conductance and soot mass loading is reported in Figs. 22 – 24. First, the gravimetric measurements are discussed, followed by the transmission measurements, and then a comparison of the trends of the two methods.

In Fig. 22, the gravimetric soot mass loading measurements on each board are plotted as a function of the average conductance across all four comb patterns. Gravimetric soot mass loading was measured for all conditions previously discussed except the horizontal orientation. The conductance plotted in each series comes from a deposition experiment without foil disks on the board surface at the same conditions. The experiment from which the *G* data are taken is indicated in the legend. Repeat experiments for the conditions of 3 SLM and ΔT = 200 °C are plotted with different symbols in blue using the same *G* values. Figure 22 includes the final as well as intermediate measurements of *G* with proportionately scaled mass loadings at 1200 s, 1800 s, 2400 s and 3000 s. The measurements at 600 s are excluded because the *G* measured at that time is not consistently above zero. The conductance error bars show the expanded uncertainty based on the four measurements averaged on each board. The uncertainty in gravimetric mass loading (± 1 mg/m^2) is not shown because it would be smaller than the size of the data symbols in the figure. Despite the varying conditions tested and the need for separate experiments to measure mass loadings and *G*, the data are clustered around a clear trend.

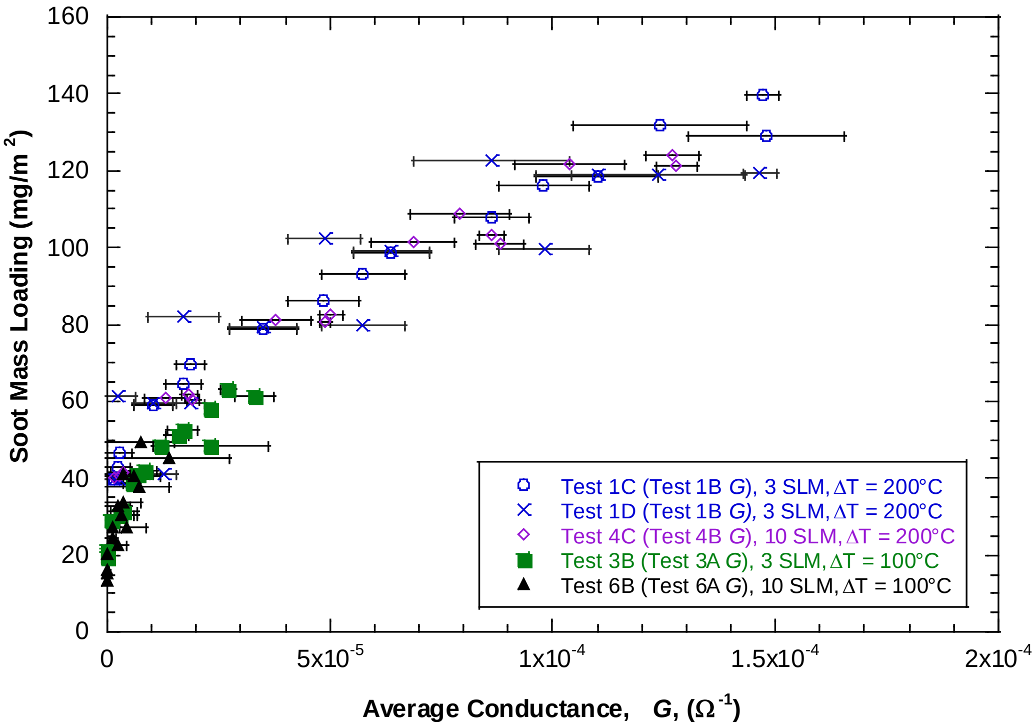

Fig. 22. All gravimetric soot mass loadings as a function of final and intermediate *G*. Conductance error bars are shown for a 95 % confidence level.

Figure 23 shows the transmission mass loading versus *G* on each comb pattern for ΔT = 200 °C at both orientations and flowrates, with experiments at the same conditions plotted together. Figure 24 shows the transmission mass loading versus *G* for ΔT = 100 °C at both flowrates in the same plot. All final values and intermediate values are plotted in the graphs in Figs. 23 and 24, except for some 600 s intermediate measurements of *G* that are below zero. The red open symbol data sets are from early experiments in which intermediate current measurements were taken without stopping the soot exposure.

Error bars for *G* are shown for measurements where the expanded uncertainty is larger than the size of the symbols. Only intermediate *G* measurements from the red data sets have expanded uncertainties that are larger than the width of the symbols. The uncertainty in *G* for the transmission graphs is smaller than for the gravimetric graphs because the *G* data in Figs. 23 and 24 represent measurements on a single comb pattern rather than an average over four combs in Fig. 22. The uncertainty in transmission soot mass loading, ± 10 mg/m^2, applies to all soot mass loading measurements in Figs. 23 and 24, but is shown on only one point in each graph for clarity. The uncertainties cannot fully account for the large scatter seen for the transmission mass loading graphs, but the scatter is similar regardless of the conditions. The scatter is likely a result of unquantified uncertainties introduced in wiping the soot off of the surface and in removing the soot from the tissue into the solution. These types of errors would likely result in an underestimation of the soot mass loading because soot particles could be lost during the multiple step process. Despite the wide scatter in the data points, the transmission data appear to have similar trends to each other and to the gravimetric data in Fig. 22.

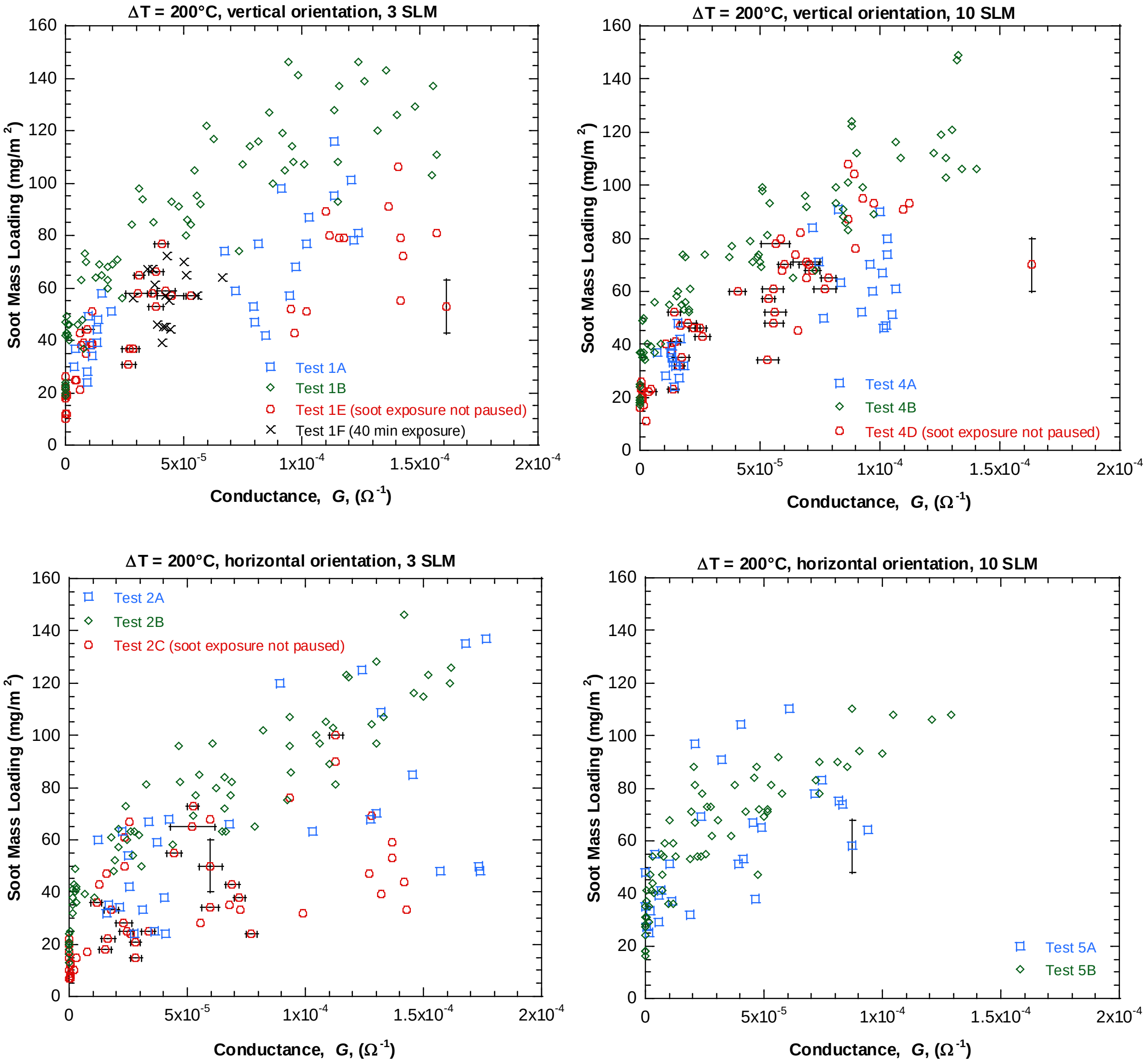

Fig. 23. Transmission soot mass loadings as a function of final and intermediate *G* for ΔT = 200 °C in (top) vertical orientation and (bottom) horizontal orientation for (left) 3 SLM and (right) 10 SLM. Soot mass loading uncertainty is constant (± 10 mg/m^2), and the error bar is shown on only one point on each graph for clarity. Conductance error bars for a 95 % confidence level are shown if they are larger than the symbol.

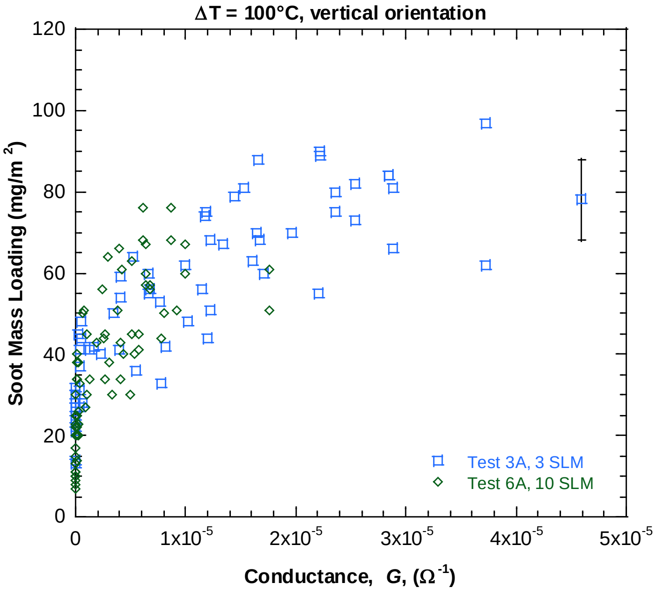

Fig. 24. Transmission soot mass loadings as a function of final and intermediate *G* for ΔT = 100 °C for 3 SLM and 10 SLM. Soot mass loading uncertainty is constant (± 10 mg/m ^{2}), and the error bar is shown on only one point on each graph for clarity.

A comparison between the gravimetric and transmission data is given in Fig. 25 along with best fit lines for the correlations between soot mass loading and conductance. All of the gravimetric data from Fig. 22 is plotted in blue open symbols. The transmission data in the black closed symbols includes the data from all of the conditions plotted in Figs. 23 and 24, excluding the intermediate data and excluding the experiments in red for which the soot exposure was not paused. A power fit trendline is found for each of the measurement methods. The R^2 correlation coefficient is much closer to 1 for the gravimetric data compared to the transmission data. Also, the standard deviation of the data from the gravimetric trendline is 11, and standard deviation from the transmission trendline is 22. These results are consistent with the significant transmission scatter seen in the previous graphs. The greater scatter for transmission data was attributed to the stated transmission uncertainties as well as errors inherent to the transmission method that would be expected to under-predict the mass loading. The comparison in Fig. 25 supports the hypothesis that the transmission method tends to under-predict mass loading because there are a significant number of transmission data points below the gravimetric data. In other words, the gravimetric data are clustered toward the top of the range of the transmission data. The transmission trendline is also affected, since the gravimetric trendline exponent is 0.26, and the transmission trendline exponent is much lower, 0.18.

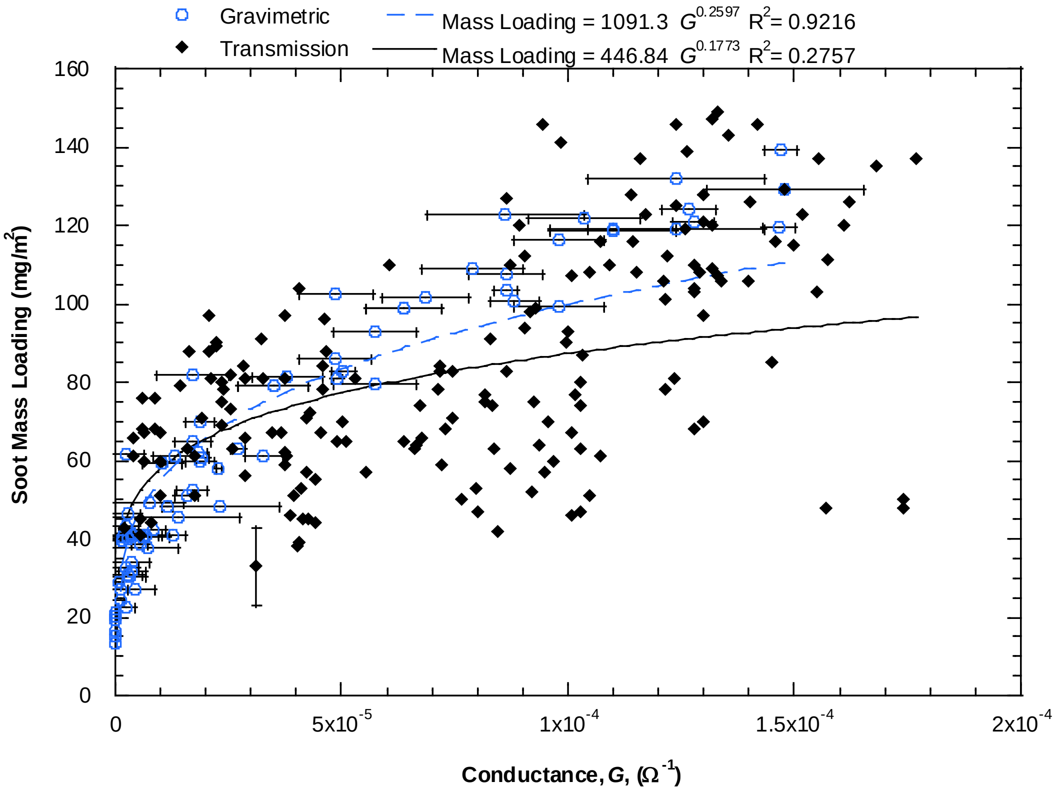

Fig. 25. Soot mass loadings as a function of *G* for the gravimetric method (final and intermediate measurements) and transmission method (final measurements excluding tests 1E, 2C and 4D). Transmission mass loading uncertainty is ± 10 mg/m^2 and shown on only one point for clarity. Conductance error bars are shown for a 95 % confidence level.

4.3 Deposition and Thermophoretic Velocities

The experimental deposition velocity, v_{dep}, is calculated from the measured soot mass loading averaged for all locations within a test and the average incoming soot concentration, C_p, using Eq. (2). The C_p values at standard conditions given in Table 3 are adjusted to account for the volume at the actual flow temperature in the channel. This temperature is approximated by the average of the flow temperatures measured at the inlet and outlet, given in Table 4 as T_p.

Table 4. Thermal Measurements for v_{dep} and v_{th} Calculations

	ΔT = 200 °C				**ΔT = 100 °C**	
	Vertical		**Horizontal**		**Vertical**	
Channel flow (SLM)	3	10	3	10	3	10
Measured ∇T (°C/cm)	197.4	197.0	195.4	195.1	103.9	104.1
Measured T_p (°C)	69	77	69	53	46	57

The average v_{dep} from each experiment is compared to the theoretical v_{th} determined from Eq. (1). Because of the linear temperature gradient across the channel, the ∇T for the calculation of v_{th} is determined based on the surface temperature measurements described in Sec. 2.2. The average of the temperatures measured at the inlet and outlet is also used to estimate the particle temperature, T_p. The variation of K_{th} with a range of particle sizes (0.01 µm to 2.5 µm) and T_p (45 °C to 85 °C) was explored in Fig. 26. The K_{th} values in Fig. 26 are mostly less than 0.55 because the Kn is less than or close to 1. Around $D_p = 0.035$ µm, K_{th} becomes 0.55 because Kn has increased to 4, indicating the free molecular regime. The plot shows that within the ranges considered, the dependence on temperature is small compared to the dependence on particle size. Therefore, the temperature chosen as T_p does not have a major effect on K_{th}. Table 4 reports ∇T and T_p for the different cases of flow and ΔT. A K_{th} of 0.55 was used to for the v_{th} calculation.

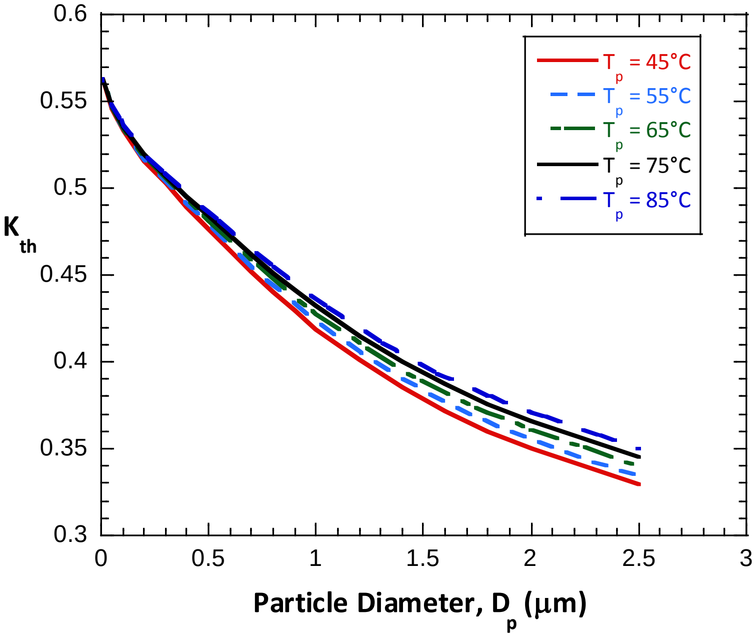

Fig. 26. Variation of the thermophoretic coefficient with particle size for different temperatures.

The calculated v_{th} is compared with the measured v_{dep} in Fig. 27, with the dashed line representing correspondence between the two velocities. Each symbol represents one experiment, with different color symbols representing gravimetric and transmission based soot mass loadings. The transmission data are further separated into vertical and horizontal data. The v_{dep} error bars reflect the combined expanded uncertainties, with the largest contribution coming from the measurement of incoming C_p. The average v_{dep} uncertainty is ± 32 % for the transmission data, ± 30 % for the gravimetric data using TEOM-based C_p, and ± 13 % for the gravimetric data using filter-based C_p. The combined uncertainty in v_{th} is ± 14 %, using an estimated uncertainty of 10 % in the temperature gradient and an estimated uncertainty of 15 °C in T_p.

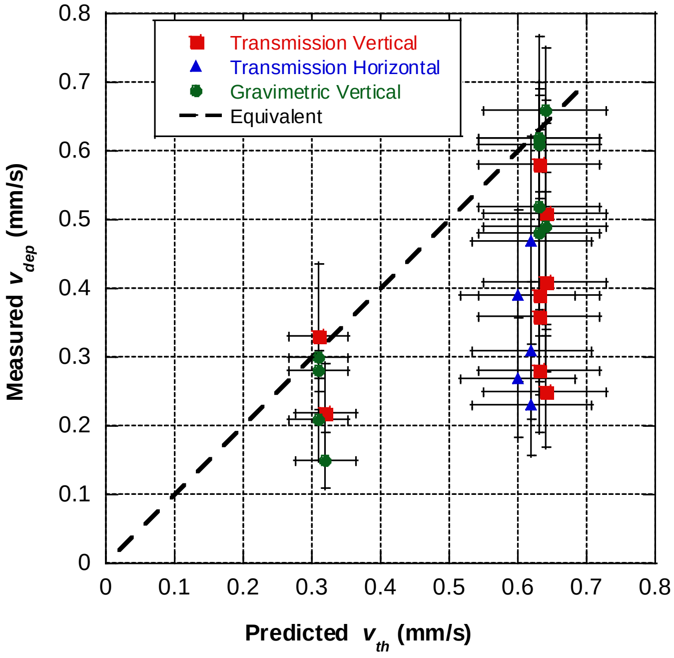

Fig. 27. Deposition velocity calculated from the final average soot mass loading and the incoming C_p versus v_{th} predicted from the measured temperature gradient for each experiment. Error bars are shown for a 95 % confidence level for both v_{dep} and v_{th}.

The primary factor that affects thermophoretic velocity is the applied temperature gradient of the exposure, regardless of the channel flowrates, orientation or fuel flowrate for each case. The cases with ΔT of 200 °C are clustered around 0.6 mm/s, and the cases with ΔT of 100 °C are clustered around 0.3 mm/s. The transmission-based horizontal v_{dep} are in the same range or lower than the data for vertical v_{dep}, so there does not appear to be a significant contribution from gravitational deposition in these experiments. Considering the experimental uncertainties, the gravimetric based v_{dep} in green is the data set that most consistently matches the predicted v_{th}. The error bars of only two gravimetric data points (with v_{dep} = 0.15 mm/s and 0.22 mm/s) do not overlap the equivalency line. These points are for ΔT of 100 °C in the vertical orientation. A closer look at the four spatial mass measurements in these two experiments shows that the mass deposited on the farthest upstream foil target is more than 20 % lower than the average mass on the three downstream targets. This level of variation between the first and final three targets is unusual in the observed data sets, and this one lower value causes the average deposition velocity to be skewed low. While a few of the transmission based v_{dep} in red and blue are close to their predicted v_{th}, the transmission data points are more scattered with most lying below the equivalency line. Any underestimation of the soot mass loading, due to mass losses in the transmission measurement process, would lead to an underestimation of the transmission-based v_{dep} as well.

5. Conclusion

The flow channel provided a uniform deposition mechanism to study the effectiveness of a conductometric gauge for soot deposition. Deposition from gravitational settling was found to be insignificant compared to thermophoretic deposition. This was most likely due to large particles, which are more affected by gravitational settling, being deposited upstream of the channel in turns and area changes. Additionally, the residence time of particles from the burner to the channel exit was only a few seconds and not enough for particle agglomeration to be important. Two methods were employed to determine the mass loading of soot deposition. The gravimetric method was more precise for obtaining the mass loading, with a standard deviation from the trendline that was half of that for the transmission method. The transmission method had the advantages of soot deposition being measured for the same experiment in which conductance was simultaneously measured, and offering more spatial measurement locations than the gravimetric method. Although measurements of soot mass loading showed significant variability with the transmission method, the variability was quantified and the trends were similar between the two methods. Additionally, it was shown it is possible to correlate conductance to soot mass deposited for the types and quantities of soot tested. If the deposition parameters were significantly changed, the design of conductometric gauge arms and spacing could be altered to allow for a different range of soot properties or thermal conditions. The calculated deposition velocities from gravimetric measurements compared well with the predicted thermophoretic velocities (using K_{th} = 0.55) within the experimental uncertainties. The transmission based measurements of deposition velocity were generally lower than the same thermophoretic velocities beyond the quantified experimental uncertainties. Some of the error in transmission based data was attributed to underestimation of the soot mass loading from mass losses during the transmission measurement method. The deposition velocities predicted by FDS were lower than the predicted thermophoretic velocities and most of the gravimetric measurements of deposition velocity, even for the smallest particle diameter simulated. The underprediction of FDS is likely due to two factors. The first is that FDS currently only applies thermophoresis to aerosol particles in grid cells adjacent to walls. The second is the lower than expected temperature gradient calculated at the wall. Additional effort in extending thermophoresis to cells away from the wall as well as improving the modeling of the experimental setup could improve the comparison of the FDS predictions with thermophoretic theory and the experimental measurements.

6. References

[1] Floyd J, Overholt K, Ezekoye O (2014) Soot Deposition and Gravitational Settling Modeling and the Impact of Particle Size and Agglomeration. *Proceedings of the 11th International Symposium of Fire Safety Science*.

[2] Floyd J, McDermott R (2010) Modeling soot deposition using large eddy simulation with a mixture fraction based framework. *Interflam: Proceedings of the 12th International Conference* (Interscience Communications).

[3] Floyd J (2016) A numerical investigation on the impact of modeling aerosol behaviors on the prediction of soot density in a compartment fire. *Interflam: Proceedings of the 14th International Conference* (Interscience Communications), pp 835–846.

[4] Lutic D, Pagels J, Bjorklund R, Josza P, Visser JH, Grant AW, et al. (2010) Detection of Soot Using a Resistivity Sensor Device Employing Thermophoretic Particle Deposition. *J of Sensors* 2010:421072. https://doi.org/10.1155/2010/421072

[5] Hagen G, Feistkorn C, Wiegärtner S, Heinrich A, Brüggemann D, Moos R (2010) Conductometric Soot Sensor for Automotive Exhausts: Initial Studies. *Sensors* 10(3):1589–1598. https://doi.org/10.3390/s100301589

[6] Cleary T (2014) Effects of Soot Deposition on Current Leakage in Electronic Circuitry. *Proc. of the 15th Int. Conf. on Automatic Fire Detection (AUBE).*

[7] Butler KM, Mulholland GW (2004) Generation and Transport of Smoke Components. *Fire Tech* 40(2):149–176. https://doi.org/10.1023/B:FIRE.0000016841.07530.64

[8] Messerer A, Niessner R, Pöschl U (2003) Thermophoretic deposition of soot aerosol particles under experimental conditions relevant for modern diesel engine exhaust gas systems. *J of Aerosol Science* 34(8):1009–1021. https://doi.org/10.1016/S0021-8502(03)00081-8

[9] McGrattan K, Hostikka S, McDermott R, Floyd J, Weinschenk C, Overholt K (2015) *Fire Dynamics Simulator Technical Reference Guide Volume 1: Mathematical Model.* https://doi.org/10.6028/NIST.SP.1018

[10] Rosner DE, Khalil YF (2000) Particle Morphology- and Knudsen Transition-Effects on Thermophoretically Dominated Total Mass Deposition Rates From "Coagulation-Aged" Aerosol Population. *J of Aerosol Science* 31(3):273–292. https://doi.org/10.1016/S0021-8502(99)00054-3

[11] Suzuki S, Kuwana K, Dobashi R (2009) Effect of particle morphology on thermophoretic velocity of aggregated soot particles. *Int J of Heat and Mass Transfer* 52(21–22):4695–4700. https://doi.org/10.1016/j.ijheatmasstransfer.2009.05.017

[12] McGrattan K, McDermott R, Weinschenk C, Overholt K, Hostikka S, Floyd J (2015) *Fire Dynamics Simulator User's Guide 6th Edition.* https://doi.org/10.6028/NIST.SP.1019

[13] Dillner AM, Stein C, Larson SM, Hitzenberger R (2001) Measuring the Mass Extinction Efficiency of Elemental Carbon in Rural Aerosol. *Aerosol Science and Technology* 35(6):1009–1021. https://doi.org/10.1080/027868201753306778